

**OPTIMAL BACKGROUND MODEL EXTRACTION AND
IMPROVEMENT OF RTM ILLUMINATION ON BASIS
OF BORN MODELING**

A Thesis

Presented to

the Faculty of the Department of Earth and Atmospheric Sciences

University of Houston

In Partial Fulfillment

of the Requirements for the Degree

Master of Science

By

Xinglu Lin

August, 2013

**OPTIMAL BACKGROUND MODEL EXTRACTION AND
IMPROVEMENT OF RTM ILLUMINATION ON BASIS
OF BORN MODELING**

Xinglu Lin

APPROVED:

Dr. Arthur B. Weglein, Chairman,
Department of EAS and Physics

Dr. Janok Bhattacharya,
Department of Earth and Atmospheric Sciences

Dr. Fang Liu,
Department of Physics

Dr. Dan Wells, Dean
College of Natural Sciences and Mathematics

Acknowledgements

The research described in this thesis proceeds from summer of 2012 to summer of 2013. I am writing here to express my gratitude to many people who support this research.

Firstly, I would like to especially thank Prof. Arthur B. Weglein for being my thesis advisor and supporting the project all the time. I enjoy the great benefit of his technical knowledge and deep thoughts. Also, I appreciate the help and guiding through this project from Dr. Yi Luo (Saudi Aramco) who introduced me to Dr. Weglein. And I owe great gratitude to Prof. Fang Liu and Dr. Tong Fei (Saudi Aramco) for their advice and suggestions. Besides, I particularly thank Prof. Arthur B. Weglein, Prof. Janok Bhattacharya, and Prof. Fang Liu for serving as my committee members.

In addition, I am grateful to my colleagues in M-OSRP who are all team-oriented and helpful, particularly Jim Mayhan, Dr. Wilberth Herrera, Lin Tang, and Jing Wu, who help to edit this thesis. Furthermore, I would like to thank Prof. Yike Liu and Dr. Yibo Wang for providing the opportunity of an internship in the Chinese Academy of Science (CAS) and my colleagues in CAS, including Hao Hu and Peng Wang. I also sincerely thank all my friends in the Earth and Atmospheric Sciences Department, especially Heather Yao, Zhao Li, Yao Yao, and Duo Yuan.

Finally, I want to express heartfelt thanks to my parents, for their support and care. Distance between us cannot change the distance between our hearts. I receive meticulous care from them all the time.

**OPTIMAL BACKGROUND MODEL EXTRACTION AND
IMPROVEMENT OF RTM ILLUMINATION ON BASIS
OF BORN MODELING**

An Abstract of a Thesis

Presented to

the Faculty of the Department of Earth and Atmospheric Sciences

University of Houston

In Partial Fulfillment

of the Requirements for the Degree

Master of Science

By

Xinglu Lin

August, 2013

Abstract

Seismic processing methods exist that view the actual velocity configuration of the subsurface as being composed of a reference model plus a perturbation of the reference velocity. Seismic migration (or imaging) requires a velocity model to locate structure at depth. Recent progress in seismic inversion provides an estimated perturbation corresponding to a given background/reference model before imaging. This motivates the study of Born modeling, which requires as input, both a background velocity model and a perturbation in the velocity.

In this thesis, I examine the background model used in Born modeling. Different models are tested in numerical experiments in order to find the optimal choice for the background. In this study, when a Born modeling result has a minimum difference with a finite-difference (FD) modeling result, the background model used in Born modeling is called the optimal model. All the background models in my numerical experiments are generated by the Gaussian smoothing of actual models. Please note that the actual models are assumed to be known in all tests, since I am focused on forward modeling in this part of this study.

In the second section, I apply Born modeling data for reverse-time migration (RTM), the later being a processing or inversion step. Industry standard RTM is a linear and model-dependent migration method. RTM typically works with a smoothed background model to locate the imaging points using only primaries. RTM has its own technical disadvantages of producing low illumination beneath high velocity structures, such as salt bodies. To improve the illumination beneath salt, I introduce scattering by Born modeling into wave-propagations in an RTM scheme.

An improved RTM results from adding scattering into both source and receiver wavefield. I illustrate the effects of improved RTM with tests using a synthetic sub-salt model. The improved imaging result helps with delineating part of the salt boundary and salt-sediment connections. Finally, the merits and shortcomings of both original and improved RTM are analyzed.

Contents

Acknowledgements	iii
Abstract	vi
Contents	vii
List of Figures	x
List of Symbols	xiii
1 Introduction	1
1.1 Background for this thesis	1
1.2 Motivation for this thesis	4
1.3 Overview of this thesis	6
2 Basic concepts and methods	8
2.1 Discrete forward modeling	9
2.1.1 Finite-difference schemes	9
2.1.1.1 The second time derivative example	9
2.1.1.2 Accuracy of FD	11
2.1.1.3 Analysis of stability	11
2.1.2 Boundary conditions	13

2.1.2.1	Damping absorbing boundary conditions	13
2.1.2.2	Clayton absorbing boundary conditions	14
2.2	Born modeling	15
2.2.1	Scattering theory	16
2.2.2	Born approximation	17
2.3	Gaussian smoothing	18
2.3.1	Continuous Gaussian kernel	19
2.3.2	Discrete Gaussian filter	20
2.3.3	Advantages	21
2.4	Reverse-time migration basis	23
2.4.1	Cross-correlation	24
2.4.2	The concept of original RTM	24
3	Optimal background model extraction	28
3.1	Modeling methods	29
3.2	Modeling parameters	30
3.3	Tests of two-layer models	31
3.4	Tests of well-logging model and multiple layer model	33
3.5	Conclusions	34
4	Improvement of reverse-time migration (RTM) illumination	45
4.1	Sub-salt problem	46
4.2	Algorithm based on Born modeling	47
4.3	Salt model tests	50
4.4	Conclusions	54
5	Summary	56

Appendices	58
Appendix A Fourth-order accuracy FD scheme example	59
Appendix B Born modeling in space-and-time domain	61
References	64

List of Figures

2.1	Implementation of the exponential damping absorbing boundary in 2-D. A is the total length of the damping zone and D is the distance from the edge of the effective medium to the attenuation point. The damping effect on normal incidence waves is better than the effect on oblique incidence waves.	14
2.2	Standard Gaussian distribution with mean $(0, 0)$ and $\sigma = 1$ in equation (2.19) and equation (2.20), respectively.	20
2.3	Gaussian distribution on discrete grids; an averaged value defined by red points replace the value of yellow target point. C is a coefficient after normalization. The Gaussian smoother length (l) is related to the deviation term σ in formula.	23

2.4	One-dimensional cross-correlation example. Top figures plot $f_1(t)$ and $f_2(t)$ varying with time. The $f_2(t)$ (red line) slide from the left to right to cross-correlate $f_1(t)$ (blue line). The time difference caused by the position of $f_2(t)$ is called time-lag. From (a) to (e), the cross-correlation result is assigned on different time-lags. (Courtesy of Reza Arfa)	27
3.1	Different acoustic models using in experiments	36
3.2	Error variance between Born modeling and normal finite-difference data. In each diagram, the star points (*) represent the error variances calculated by an unified FD result and various Born modeling results using different background models and the red circle denotes the optimal smoothing point. The background models are generated by the Gaussian smoothing of actual models using different smoothing length ($N \times \lambda$). The background/reference models smoothed by 0.2λ , optimal length and 5.0λ are shown in each diagram.	40
3.3	Trace comparison between Born modeling and normal finite-difference data. The trace channel located at $500m$ offset. The background models are models Gaussian smoothed by a multiple (N) of λ	43
3.4	Synthetic well-logging velocity model.	44
4.1	Schematic for a ray-tracing result of a salt slab	47

4.2	Imaging principle diagram of original RTM and Born modeling based RTM	50
4.3	Original salt model (courtesy of Allied Geophysical Laboratory) and smoothed salt model	51
4.4	Original reverse-time migration result	52
4.5	Reverse-time migration result on the basis of Born modeling	53

List of Symbols

P	Total wave-field.....	9
$c(\mathbf{r})$	3-D actual velocity	9
ρ	Source term in wave-equation	9
Δt	Discrete time sample interval	10
D	Distance from effective model boundary to damping point	13
A	Length of damping zone	13
β	Damping coefficient	13
$c(x, z)$	2-D actual velocity	15
p_0	Reference wave-field (the source wave-field in RTM)	16
p_s	Scattered wave-field (the receiver wave-field in RTM)	17
$c_0(x, z)$	2-D reference velocity	16
$\alpha(x, z)$	2-D acoustic perturbation term	16
\mathbf{G}_0	Reference Green operator	18
\mathbf{V}	Perturbation operator	18
Ψ_s	Scattered wave-field (without wavelet)	18
$g(x)$	1-D Gaussian smoother kernel	19

$g(x, z)$	2-D Gaussian smoother kernel	19
σ	Deviation factor in Gaussian filter	19
l	Discrete Gaussian smoother length	21
C	Normalized coefficient	21
f, f_1, f_2	Arbitrary continuous functions	21
h	Smoothed function	21
\otimes	Cross-correlation operator	24
I	Reverse-time migration result	25
τ	Time-lag factor	24
d	Dataset	25
λ	Wavelength	28
p'_0	Reference wave-field on basis of Born modeling	48
p'_s	Scattered wave-field on basis of Born modeling	48
I'	Reverse-time migration result on basis of Born modeling	49
Δx	Discrete spatial sample interval	59
\mathbf{L}	Actual differential operator	61
\mathbf{L}_0	Reference differential operator	61
G	Matrix elements of actual Green operator	61
G_0	Matrix elements of reference Green operator	61
\mathbf{G}	Actual Green operator	62
$c_0(\mathbf{r})$	3-D reference velocity	63
$A(\omega)$	General wavelet form in frequency domain	63
$\alpha(\mathbf{r})$	3-D acoustic perturbation term	63

ω	Angular frequency	63
\hat{p}_0	Reference wave-field in frequency domain	63
\hat{p}_s	Scattered wave-field in frequency domain	63

Chapter 1

Introduction

1.1 Background for this thesis

In seismic studies, the concept of a reference or background medium originates from scattering theory, in which the actual earth can be expressed as a combination of a reference model and a perturbation of this reference, where the perturbation is defined as the difference between the actual world and the selected reference medium. Inversion works by considering the background model as the starting model, and later updating the model. The choice of a convenient background/reference model is key to the convergence of the inversion process. The Born inversion method is an example of a general inversion method, which can invert a linear perturbation. The issues in this method have been studied by Clayton and Stolt (1981), Weglein and Gray (1983), and Cohen et al. (1986). However, in this thesis I will discuss the background problems from the perspective of forward modeling. The forward modeling

method is specified as Born modeling in this thesis. The Born modeling method also calls for a background/reference velocity model and a perturbation of the reference velocity. Unlike the general modeling procedure, Born modeling assumes that the perturbation and the aperture are both small. The data resulting from Born modeling cannot be the same as the actual data, even though the true perturbation is applied in the scheme (equation (2.18)). Nevertheless, Born modeling is useful when the research interest lies in linear scattering.

Researchers have found three main approaches to generate a background model. One approach is based on velocity analysis and tomography, in which the background model is built by the smoothing of the actual model, using a low-pass filter. The Gaussian smoothing models used in this thesis project belong to this category. The other two approaches are based on automatic updating procedures, which are known as first-arrival travel-time tomography (FATT) (Dessa et al., 2004) and reflection stereotomography (Billette and Lambaré, 1998). In FATT, the first-arrival travel-times are computed with an eikonal solver using an initial smoothed actual model. Unlike FATT, the stereotomography method consists of fitting all observed data (positions, slopes and travel-times) to a dataset calculated by ray-tracing. The last two methods are designed for a faster convergence in iterative inversion. If the study is interested in applications and advantages of those two background model building methods, please refer to Prioux et al. (2009).

In order to prevent reflections from a sharp boundary, the reverse-time migration (RTM) method takes advantage of smoothing the actual model. The original RTM concept is a velocity model-dependent method, which can migrate two-way waves in

depth using the reverse-time backward propagated wave-field (Baysal et al., 1983; McMechan, 1983; Whitmore, 1983). The smoothed background model is inserted into the RTM algorithm/method as the velocity model for migration. In the original RTM, the waves propagating in a background without reflection are imaged using the primaries in the data. For this reason, considerable effort has been made to remove ghosts (Weglein et al., 2002; Mayhan and Weglein, 2013), internal multiples (Araújo et al., 1994) and free-surface multiples (Dragoset et al., 2010; Zhang and Weglein, 2005) in order to obtain a primaries only dataset. In recent years, researchers noticed the illumination problem under salt structures (O'Brien and Gray, 1996; Rosenberg, 2000) and then turned their attention to the imaging of multiples, which cannot be handled by the current linear migration schemes, e.g., original RTM and Kirchhoff migration.

In recent years, in order to solve the sub-salt problem, Fleury and Vasconcelos (2010) proposed a non-linear imaging condition. Breaking the convention of using non-reflection wave-fields which are propagated in a smoothed velocity model, they perturbed the source and receiver wave-fields using an estimated perturbation by ISS. This initial algorithm works in the frequency domain. In Fleury and Snieder (2011), the time domain version of this work is presented, where the new contribution to the imaging is the autocorrelation of the perturbed scattered field, denoted i_s . This non-linear image i_s is added to the original linear image in a numerical synthetic example of a 2-D sub-salt model. Extending these works, in this thesis I apply Born modeling into a RTM scheme to get perturbed wave-fields for imaging multiples.

1.2 Motivation for this thesis

The criterion of selecting the smoothed background model has been rarely tested or discussed. Researchers in industry apply low-pass filters, such as the Gaussian filter and the average filter, to the actual model to generate a background/reference model, which is the required input for Born modeling or imaging. In this case, two questions arise when studying Born modeling. 1) Does the Born modeling have the ability to reconstruct the primaries in the data? In principle, Born modeling only takes care of the first-order scattering as a linear truncated Born series. This means that Born modeling has no chance of perfectly reconstructing any single event in the dataset even if the true perturbation is used. 2) Which kind of background gives Born modeling the best chance of recovering desired result? To answer this question, 1.5-D Born modeling tests will be shown in this thesis to illustrate the importance of selecting an optimal background model for Born modeling.

Another challenge comes from migration (or imaging) work. As mentioned in section 1.1, RTM faces the challenges of low illumination under a salt-body or high-velocity layer. The goal of lightening the area of interest, like the salt-sediment connections, attracts many people in industry (Fei et al., 2010). Interpreters are especially interested in salt flank and connections, where potential reservoirs can exist. Toward this goal, geophysical researchers have started to think about how to include more non-linear events into the RTM scheme, as in Fleury and Snieder (2011). It is an intuitive and natural way to introduce linear scattering by Born modeling in a RTM scheme, which is an attempt for using multiply scattered waves to perform imaging.

To summarize, there are two major interests in this thesis. One is extracting the optimal background/reference model for Born modeling through numerical tests. The other is combining Born modeling and RTM as a means of illuminating the sub-salt for imaging.

1.3 Overview of this thesis

The organization in this thesis is as follows: starting with chapter 2, I will revisit the basic concepts and methods which are relevant to this project. For example, I will introduce fundamental knowledge for this thesis, like scattering theory, the Born approximation, RTM, etc. Also, basic numerical methods will be introduced to prepare for the implementations, including details of discrete forward modeling and Gaussian smoothing filtering.

In chapter 3, I will start with the process of extracting the optimal background model generated by Gaussian smoothing for different models. The examples in this chapter assume knowledge of the actual models to avoid the need for perturbation inversion. So the experiments are mainly about how to choose the background model used in research work. In the conclusions, the regularity of selecting an optimal background model and its understanding will be discussed.

Chapter 4 is devoted to the improved RTM method based on Born modeling and numerical tests of both the original and the improved RTM. The original RTM requires a migration model, but not every detail in the earth. In order to deal with the issue of low illumination under sub-salt, I add more information by using the perturbation term described in section 4.1. In practical work, the perturbation can be inverted by linear ISS inversion. However, to simply test the migration algorithm, I use the difference between the actual model and the background model as the perturbation in the numerical tests. After the introduction of the improved RTM, the imaging result will be used to illustrate the effects of the improved method in section 4.2. From the results, the advantages and disadvantages of both migration

methods can be inferred. Furthermore, section 4.3 explores the reason behind the higher illumination beneath a salt-body and new artifacts in deep depths.

Finally, chapter 5 provides a summary of all the results in chapter 3 and chapter 4, including the descriptions and analysis of results. Also, topics for further research in these directions will be discussed.

There are two appendices. In the first appendix, the fourth-order accuracy finite-difference scheme in section 2.1.1 will be derived in detail. In the second appendix, I deduce the Born modeling equation (2.18) in the time domain from the Born term in the frequency domain.

Chapter 2

Basic concepts and methods

In this chapter, the main concepts for this thesis and their computational implementation will be discussed. In the first section, discrete numerical methods for forward modeling will be introduced in detail, including the basic finite-difference scheme (FD) and the boundary conditions. Section 2.2 will briefly review the concepts of scattering theory and Born modeling. In section 2.3 I will revisit the concept of continuous and discrete Gaussian filters, since these kind of low-pass filters will be used for generating the background model. Finally, section 2.4 contains a retrospect of the original RTM algorithm.

2.1 Discrete forward modeling

2.1.1 Finite-difference schemes

The conventional numerical method - finite-difference (FD) (Alford et al., 1974)- provides a scheme for us to discretize a differential equation, like a wave-equation. FD solutions applied in the wave-equation are pervasive in seismic forward modeling (Kelly and Marfurt, 1990) and imaging (Bording and Lines, 1997). The definition of a first derivative can be given as

$$f'(x) = \lim_{h \rightarrow 0} \frac{f(x+h) - f(x)}{h}. \quad (2.1)$$

According to this definition of derivative, the increment h is approached to zero, in other words, it should be infinitesimally small. However, in a computer the derivative $f'(x)$ is approximated using a small, but finite increment. The value of FD provides an approximation for the local value of the derivative, which depends on the values at neighboring points. These neighborhoods are located at a finite (but small) distance from the point where the derivative is being calculated.

2.1.1.1 The second time derivative example

The acoustic wave equation can be written as

$$\nabla^2 P(\mathbf{r}, t) - \frac{1}{c^2(\mathbf{r})} \frac{\partial^2 P(\mathbf{r}, t)}{\partial t^2} = -\rho(\mathbf{r}_s, t), \quad (2.2)$$

where P is the pressure wave-field, ρ represents the source distribution, \mathbf{r} is the field vector, and \mathbf{r}_s is the known source position vector. Both approximate the

Laplace term and the second time derivative of pressure in equation (2.2), can be approximated in FD.

The second time derivative in equation (2.2) is a particularly good example to show how FD works on differential equations. In order to use the neighborhood points to estimate the time differential term, researchers always use a Taylor series expansion of P . This backward finite-difference requires the value of the wave-fields at previous time samples. Let us define the Δt of the time sample increment, P of a wave-field, P' of a first time derivative of P , P'' of a second time derivative of P , etc. Two Taylor expansions can be shown as,

$$P(t - \Delta t) = P(t) - P'(t)\Delta t + P''(t)\frac{\Delta t^2}{2} - P'''(t)\frac{(\Delta t)^3}{6} + \mathcal{O}(\Delta t^4), \quad (2.3)$$

$$P(t - 2\Delta t) = P(t) - P'(t)2\Delta t + P''(t)\frac{(2\Delta t)^2}{2} - P'''(t)\frac{(2\Delta t)^3}{6} + \mathcal{O}((2\Delta t)^4). \quad (2.4)$$

Upon multiplication of expansion 2.3 by two, followed by subtraction of expansion 2.4, we arrive at the following FD approximation for the second derivative in time of the wave-field. which is

$$P''(t) = \frac{P(t - 2\Delta t) - 2P(t - \Delta t) + P(t)}{(\Delta t)^2} + \mathcal{O}(\Delta t). \quad (2.5)$$

This procedure can also be used for estimating the derivatives in the Laplace term. The term $\mathcal{O}((\Delta t))$ of equation (2.5) indicates that the error is proportional to the time sample interval, which determines the order of FD accuracy. This accuracy analysis will be discussed in the next subsection.

2.1.1.2 Accuracy of FD

The example of second derivative with respect to time illustrates the concept of accuracy of FD. Using equation (2.3) and equation (2.4), the same algebraic steps in subsection 2.1.1.1 can give

$$\frac{P(t - 2\Delta t) - 2P(t - \Delta t) + P(t)}{(\Delta t)^2} - P''(t) = -P'''(t)\Delta t + \mathcal{O}(\Delta t^2). \quad (2.6)$$

The right-hand side of equation (2.6) is called the truncation error. By definition, the order of a FD scheme is the lowest power of interval (Δt) in the truncation error. So the first-order accuracy backward FD is selected in this thesis to estimate the second time derivative term. Besides, the 8th order accuracy central FD is chosen to discretize the Laplace term in the wave-equation. An example of a fourth order accuracy FD scheme is discussed in appendix A.

However, a higher accuracy order FD cannot guarantee a better approximation due to a large value of higher derivative ($P'''(t)$) in leading truncation terms or an instable FD numerical system.

2.1.1.3 Analysis of stability

Stability of a FD scheme means that the truncation error caused by a small change in the numerical solution is bounded. It is necessary to be aware of the stability issue in numerical experiments, otherwise the computer fails to produce an accurate solution. The stability analysis for FD of partial differential equation was originally developed by John von Neumann. Recent research by Mufti (1990) and Wu et al. (1996) provides the stability criteria for the FD solutions of the 3D wave-equation.

The criterion will be briefly discussed in this section and directly applied in later numerical tests without derivation. Please refer to Mufti (1990), Wu et al. (1996), and Press et al. (1986), for a more detailed discussion of the criterion.

For the numerical solution of the wave-equation, the parameters can be set as a spatial sampling interval with value h ($\Delta x = \Delta z = h$), a temporal sampling interval Δt , and a velocity c . Then the stability condition for FD computation can be expressed as

$$\frac{c\Delta t}{h} \leq \sqrt{\frac{a_1}{a_2}}. \quad (2.7)$$

In the condition (2.7), a_1 is the summation of absolute value of weight for the FD approximation of the second time derivative and a_2 is the summation of absolute value of weight for the FD solution of the Laplace term. For instance, the experiments in this thesis use first-order backward FD for the time derivative and 8th order central FD for the space derivative. The time derivative approximation use the weights as $(1, -2, 1)$ (equation (2.5)), so it is easy to give $a_1 = 4$. The weights for a 8th accuracy central FD of 2-D Laplace operator can provide the value of a_2 . The stability condition used in FD implementation in this project is

$$\frac{c\Delta t}{h} \leq 0.7843. \quad (2.8)$$

In all later numerical experiments, the parameters of spatial or temporal intervals and localized velocities are chosen to satisfy this criterion of stability.

2.1.2 Boundary conditions

In a finite square modeling area, the four boundaries can reflect waves back to the effective computational zone, acting as walls. This kind of boundary reflection can bring an alias in later imaging work. In order to attenuate the boundary-related reflections, the damping absorbing boundary condition and the Clayton absorbing boundary conditions are both applied in my numerical tests. The conditions and parameters described in the following sections remain in forward modeling and imaging.

2.1.2.1 Damping absorbing boundary conditions

Damping zones are the artificial boundaries in modeling, which reduce the wave strength over a grid region (figure 2.1). The wave-fields in the damping zones are exponentially decayed by multiplying a traditional damping factor. The formula of damping absorbing factor can be expressed as $e^{-\beta \cdot D/A}$, where D is the grid distance from effective model boundary to the damping point, A is the entire length of one-side damping zone and β is a damping coefficient (figure 2.1). A is an input parameter, which defines the size of a damping zone separated from the effective computational area. Furthermore, the damping coefficient controls the damping acceleration from the effective edge to the damping zone edge. If the value of β is not proper for the system, the boundary of the effective zone can play a role of a new wall, which enhance the boundary reflections.

The exponential damping absorbing factor is simple but costly when it is applied in a 3-D FD scheme. Another issue is the less effective attenuation of radiating waves,

because $\frac{D}{A}$ in the damping factor is designed for the normal incidence.

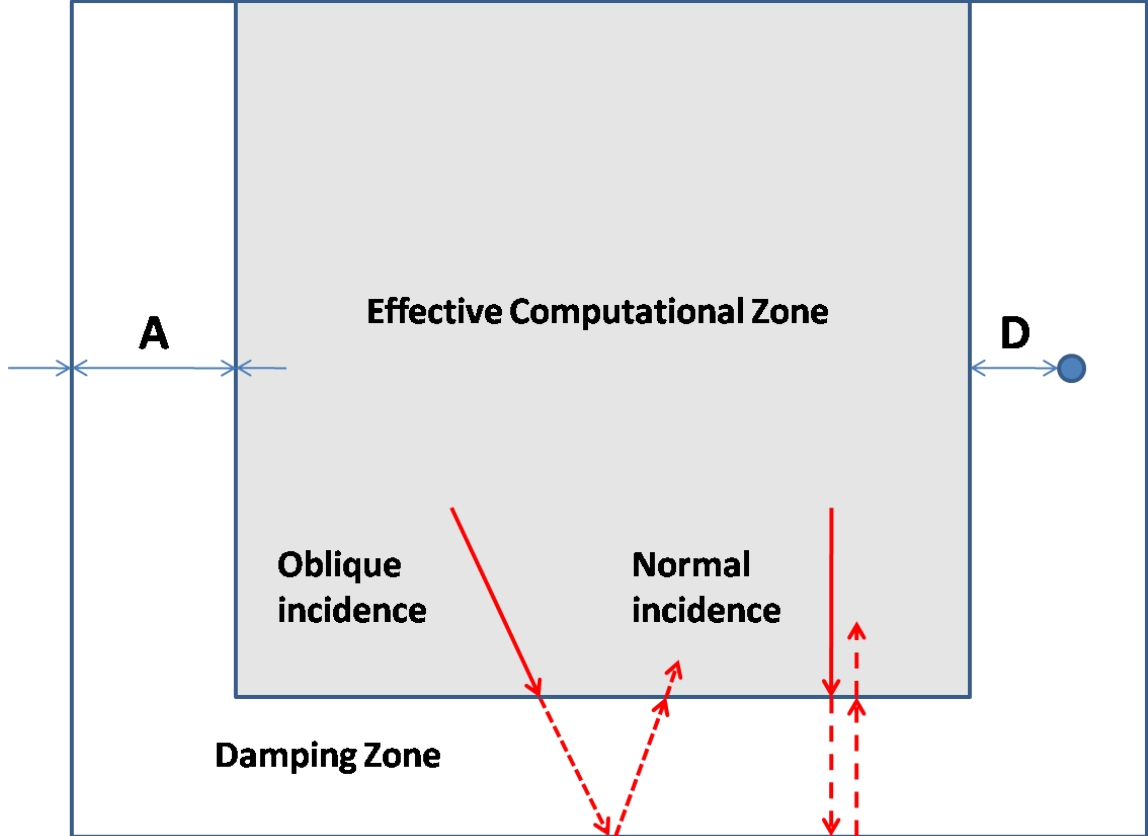


Figure 2.1: Implementation of the exponential damping absorbing boundary in 2-D. A is the total length of the damping zone and D is the distance from the edge of the effective medium to the attenuation point. The damping effect on normal incidence waves is better than the effect on oblique incidence waves.

2.1.2.2 Clayton absorbing boundary conditions

Another boundary condition is the traditional Clayton absorbing boundary condition, which was developed by Clayton and Engquist (1980). The reason for introducing this boundary condition into FD scheme is that the grid points on the edge

of a model do not have enough neighboring points to obtain the approximate value. Also, dealing with edge points is necessary to attenuate the boundary reflection. The Clayton absorbing boundary condition B1 (Clayton and Engquist, 1980) is applied on the three edges of the computational grid. Dealing with the edge of left and right boundaries, B1 actually interpolates the values of edge points with first gradient relation along x-dimension as

$$\frac{\partial P(x, z, t)}{\partial x} - \frac{1}{c(x, z)} \frac{\partial P(x, z, t)}{\partial t} = 0. \quad (2.9)$$

Please note that the spatial derivative in equation (2.9) changes to a first derivative of P with respect to z for dealing with the edges of top and bottom boundaries, as

$$\frac{\partial P(x, z, t)}{\partial z} - \frac{1}{c(x, z)} \frac{\partial P(x, z, t)}{\partial t} = 0. \quad (2.10)$$

The application of Clayton absorbing boundary reduces the energy of the surface-related reflections. In this case, I assume that the surface-related reflections do not appear in synthetic data.

2.2 Born modeling

In this section, I will review the basic concepts of scattering theory and Born modeling. In addition, since the first topic is on the extraction of the optimal background, the Gaussian filter will be discussed as a tool to generate smoothed background/reference models.

2.2.1 Scattering theory

Scattering theory is a framework for studying the scattering wave and it separates the actual medium into two contributions. One of them is called the defined background medium or reference medium. The other contribution is characterized by a perturbation operator, which corresponds to the difference between actual and background medium. Assuming that the background/reference medium is defined as a velocity model $c_0(x, z)$ in a 2-D case, I begin with introducing the definition of perturbation $\alpha(x, z)$ as

$$\frac{1}{c^2(x, z)} = \frac{1}{c_0^2(x, z)}(1 - \alpha(x, z)). \quad (2.11)$$

P and P_0 are defined as the wave-fields which are propagated in the actual and reference medium, respectively. The wave equations that describe these two wave-fields can be written as,

$$\nabla^2 P(x, z, t) - \frac{1}{c^2(x, z)} \frac{\partial^2 P(x, z, t)}{\partial t^2} = -\rho(x_s, z_s, t), \quad (2.12)$$

$$\nabla^2 p_0(x, z, t) - \frac{1}{c_0^2(x, z)} \frac{\partial^2 p_0(x, z, t)}{\partial t^2} = -\rho(x_s, z_s, t), \quad (2.13)$$

where $c(x, z)$ is the velocity model of the actual medium, $c_0(x, z)$ is the velocity model of the reference medium and ρ is the source. Scattering theory helps us separate the actual earth into a reference medium and a corresponding perturbation. The reference wave-field P_0 is the response to the source ρ in the reference medium. Combined with the perturbation definition in equation (2.11), the difference between equation (2.12) and equation (2.13) can cancel the contribution of source term ($\rho(x_s, z_s, t)$).

The final equation can be obtained as

$$\nabla^2(P(x, z, t) - p_0(x, z, t)) - \frac{1}{c_0^2(x, z)} \frac{\partial^2(P(x, z, t) - p_0(x, z, t))}{\partial t^2} = -\frac{\alpha(x, z)}{c_0^2(x, z)} \frac{\partial^2 P(x, z, t)}{\partial t^2}. \quad (2.14)$$

From the above equation, if the difference between P and p_0 is defined as p_s , this wave-field p_s is the response to the perturbation. In other word, scattering theory separate not only the actual earth $c(x, z)$, but also the wave-field P into reference wave-field and scattered wave-field. p_s is named after the scattered wave-field, which satisfies

$$P(x, z, t) = p_0(x, z, t) + p_s(x, z, t). \quad (2.15)$$

Please note that the reference medium can be chosen as any velocity model in scattering theory, such as a constant velocity model. However, the Gaussian smoothed models are considered as background/reference models in this thesis for the purpose of RTM and Born modeling.

2.2.2 Born approximation

Born approximation is a linear scattering approximation in the condition that the perturbation and the aperture of source-receiver are both small. Born modeling utilizes the idea of this approximate method in forward modeling and simplifies wave scattering as first-order linear scattering. If the perturbation is small enough in seismic wave propagation, Born modeling can be applied. Therefore, some steps are shown as following to derive the 2-D approximate modeling. Firstly, substituting

$\alpha(x, z)$ in equation (2.11) and equation (2.15) into equation (2.12) gives,

$$[\nabla^2 - \frac{(1 - \alpha(x, z))}{c_0^2(x, z)} \frac{\partial^2}{\partial t^2}](p_0(x, z, t) + p_s(x, z, t)) = -\rho(x_s, z_s, t). \quad (2.16)$$

A subtraction between equation (2.16) and equation (2.13) provides that

$$\nabla^2 p_s(x, z, t) - \frac{1}{c_0^2(x, z)}(1 - \alpha(x, z)) \frac{\partial^2 p_s(x, z, t)}{\partial t^2} = -\frac{\alpha(x, z)}{c_0^2(x, z)} \frac{\partial^2 p_0(x, z, t)}{\partial t^2}. \quad (2.17)$$

The small perturbation $\alpha(x, z)$ can be ignored on the left side and then the equation is simplified as,

$$\nabla^2 p_s(x, z, t) - \frac{1}{c_0^2(x, z)} \frac{\partial^2 p_s(x, z, t)}{\partial t^2} = -\frac{\alpha(x, z)}{c_0^2(x, z)} \frac{\partial^2 p_0(x, z, t)}{\partial t^2}. \quad (2.18)$$

In this case, the term left on the right-hand side $-\frac{\alpha(x, z)}{c_0^2(x, z)} \frac{\partial^2 p_0}{\partial t^2}$ acts as the source term.

Equation (2.18) implemented by FD is the foundation modeling scheme in this thesis.

Using scattering theory in the frequency domain, Born approximation points to the first linear term in the Born series, which can be expressed as $\Psi_s = \mathbf{G}_0 \mathbf{V} \mathbf{G}_0$ (Weglein et al., 2003). Ignoring the small perturbation, equation (2.18) is equal to the Born approximation result in the frequency domain. This equivalence is proved in appendix B.

2.3 Gaussian smoothing

The previous introduction of scattering theory clarifies the concepts of reference/background model. However, RTM requires elimination of any reflections produced by the sharp-background velocity model, and therefore a smoothing of this reference model becomes necessary. Plenty of smoothing filters have been developed in the field of

digital image processing, like the mean average filter and the Gaussian filter. These low-pass filters can smooth the actual velocity model, as a tool of generating migration models. The 2-D Gaussian filter is chosen as the way of smoothing in numerical tests.

2.3.1 Continuous Gaussian kernel

In a similar fashion to a mean averaging method, a Gaussian smoother establishes a bell-shaped distribution to average neighborhood points (Figure 2.2). The mathematical definition of 1-D and 2-D Gaussian kernels provide the distributions. In the 1-D case, the kernel is only related to one direction x and the deviation term σ as,

$$g(x) = \frac{1}{\sqrt{2\pi}\sigma} e^{-\frac{x^2}{2\sigma^2}}. \quad (2.19)$$

Besides, the Gaussian kernel is symmetric in the 2-D (x, z) domain in the following,

$$g(x, z) = \frac{1}{2\pi\sigma^2} e^{-\frac{x^2+z^2}{2\sigma^2}}. \quad (2.20)$$

The deviation factor σ determines the width of a continuous Gaussian kernel. In other word, a larger σ means more spread and intensive smoothing.

The 2-D continuous Gaussian kernel is normalized distribution, which can be proved by the integral of the kernel over x and z . The integrand can be written as

$$\begin{aligned} & \iint \frac{1}{2\pi\sigma^2} e^{-\frac{x^2+z^2}{2\sigma^2}} dx dz \\ &= \int \frac{1}{2\pi\sigma^2} \sqrt{2\pi}\sigma e^{-\frac{z^2}{2\sigma^2}} dz \\ &= \frac{1}{2\pi\sigma^2} \sqrt{2\pi\sigma^2} \sqrt{2\pi\sigma^2} \\ &= 1. \end{aligned} \quad (2.21)$$

In order to make this property of Gaussian filter remain, the weights in discrete Gaussian filter need to be normalized.

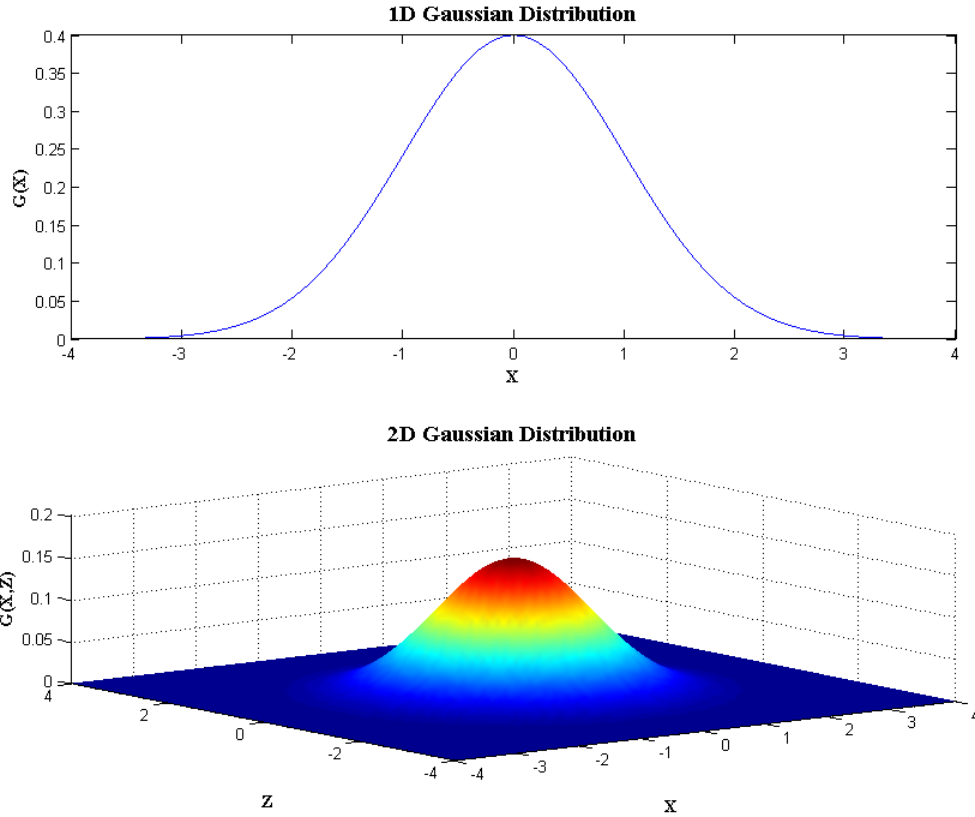


Figure 2.2: Standard Gaussian distribution with mean $(0,0)$ and $\sigma = 1$ in equation (2.19) and equation (2.20), respectively.

2.3.2 Discrete Gaussian filter

Although in principle the Gaussian kernel gives a continuous and non-zero infinite distribution, in the computer, the pixel of the Gaussian filter on grids are discrete points, shown in Figure 2.3. Hence, the stepped distance between points take the

place of continuous x, z and the filter has a finite window size.

The discrete Gaussian smoother length on grids is defined as l , which has the same meaning but the different value of σ . Because the weight approaches to zero as the point is far from the target smoothing point, the points whose exponential weight is smaller than e^{-1} on the edge and smaller than e^{-2} at the corner are truncated. This truncation gives the relation $l = 2\sqrt{2}\sigma$. In addition, the overall summation of discrete weights remains one. Then the coefficient C (figure 2.3) of the Gaussian kernel can be normalized as $C = 1/(\sum_{m=-l/2}^{l/2} \sum_{n=-l/2}^{l/2} e^{-\frac{4m^2+4n^2}{l^2}})$.

The convolution of a discrete 2-D Gaussian kernel and a function $f(x, z)$ gives a smoothed version of $f(x, z)$, which is denoted as $h(x, z)$:

$$h(n, m) = C \sum_{m'=-l/2}^{+l/2} \sum_{n'=-l/2}^{+l/2} f(n - n', m - m')g(n', m'). \quad (2.22)$$

The Gaussian smoothing kernel acts as a low-pass frequency filter which attenuates high frequency components and removes details. This kind of behavior can be detected by Fourier transformation of a Gaussian filter.

2.3.3 Advantages

The advantages of Gaussian smoothing mainly lie in two aspects: easy controlling and computational efficiency.

The degree of Gaussian smoothing is conveniently controlled by the deviation factor σ . It filters the matrix (vector) symmetrically in all directions.

The computational efficiency occurs in the implementation of high-dimensional filters using 1-D filters. This property can be shown in brief math steps from equation

(2.22),

$$\begin{aligned}
& h(n, m) \\
&= C \sum_{m'=-l/2}^{+l/2} \sum_{n'=-l/2}^{+l/2} f(n-n', m-m')g(n', m') \\
&= C \sum_{m'=-l/2}^{+l/2} \sum_{n'=-l/2}^{+l/2} f(n-n', m-m')e^{-\frac{m'^2+n'^2}{2\sigma^2}} \\
&= C \sum_{m'=-l/2}^{+l/2} e^{-\frac{m'^2}{2\sigma^2}} \left[\sum_{n'=-l/2}^{+l/2} f(n-n', m-m')e^{-\frac{n'^2}{2\sigma^2}} \right] \\
&= C \sum_{m'=-l/2}^{+l/2} e^{-\frac{m'^2}{2\sigma^2}} h'(n, m-m'). \tag{2.23}
\end{aligned}$$

The result of smoothing along one dimension is defined as $h'(n, m - m')$, which satisfies

$$h'(n, m - m') = \sum_{n'=-l/2}^{+l/2} f(n-n', m-m')e^{-\frac{n'^2}{2\sigma^2}}, \tag{2.24}$$

so that the 2-D Gaussian smoothing can be implemented with two 1-D Gaussian filters, which is faster than 2-D smoothing implementation. For example, in a 2-D Gaussian smoothing, firstly $h'(t)$ can be obtained using a 1-D Gaussian filter (equation (2.24)). And then transpose the $h'(x, z)$ to $h'(z, x)$ in order to smooth the other dimension in the same way as the first time. Finally, transpose the 2-D matrix back to get $h(x, z)$. The computational cost of Gaussian smoothing in a higher-dimension benefits from this property.

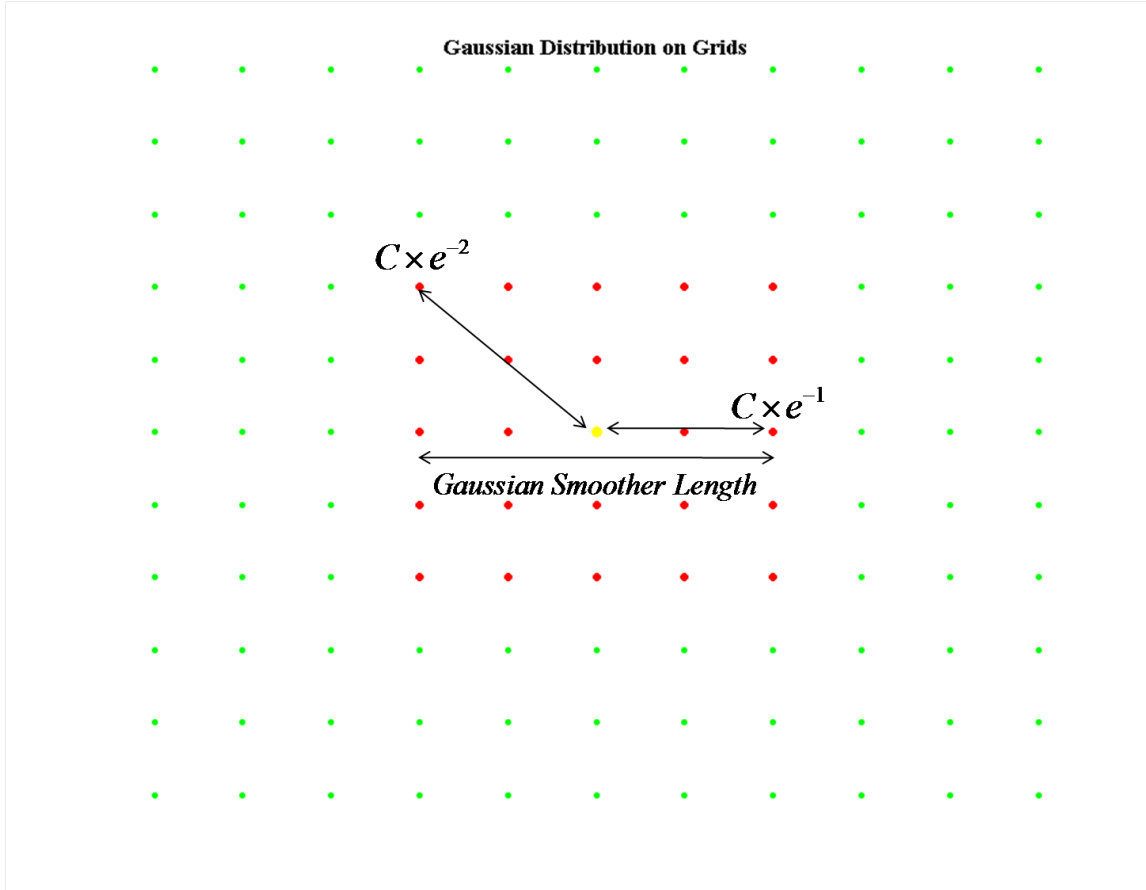


Figure 2.3: Gaussian distribution on discrete grids; an averaged value defined by red points replace the value of yellow target point. C is a coefficient after normalization. The Gaussian smoother length (l) is related to the deviation term σ in formula.

2.4 Reverse-time migration basis

Reverse-time migration (RTM) is a velocity-model dependent method, which can migrate two-way waves in depth using the reverse-time backward propagated data (Baysal et al., 1983; McMechan, 1983; Whitmore, 1983). Some ray-based migration theories are also proposed to deal with seismic data, like classical Kirchhoff migration. However, when lateral velocity varies significantly, Kirchhoff migration suffers from

difficulties in wrong imaging and severe artifacts. In this section, I will introduce the cross-correlation relation for a better understanding of the imaging condition, and then the basic RTM scheme will be revisited for the numerical tests in chapter 4.

2.4.1 Cross-correlation

Cross-correlation provides a measurement of similarity of two waveforms as a function of time-lag. The basic strategy of cross-correlation is known as a sliding dot product. If there are two continuous functions of time denoted as $f_1(t)$ and $f_2(t)$, then the correlation of these two functions is

$$f_1 \otimes f_2(\tau) = \int f_1^*(t) \cdot f_2(t + \tau) dt. \quad (2.25)$$

For a discrete function, the definite can be expressed as

$$f_1 \otimes f_2[\tau] = \sum_{t=-\infty}^{\infty} f_1^*[t] \cdot f_2[t + \tau]. \quad (2.26)$$

In these two equations, f_1^* is the complex conjugate of f_1 and τ is defined as the time-lag. In RTM scheme, the traditional imaging condition is a zero time-lag cross-correlation, which is a special case of the general cross-correlation, namely, when $\tau = 0$. In this case, the image result can be considered as a similarity of two wave-fields at zero time-lag. Figure 2.4 illustrates the concept of cross-correlation in 1-D.

2.4.2 The concept of original RTM

The idea of original pre-stack RTM is straightforward. First propagate the source function in a reference medium and store the reference wave-fields ($p_0(x, z, t)$) for all

time samples. From the receiver side, the dataset is backward propagated and then the scattered wave-field ($p_s(x, z, t)$) is provided. In the habit of industry standard, p_0 and p_s are named as the source wave-field and the receiver wave-field, respectively. Finally the image is obtained by applying a zero time-lag cross-correlation imaging condition as

$$I(x, z) = \sum_{sources} p_0(x, z, t) \otimes p_s(x, z, t), \quad (2.27)$$

which can be found in Claerbout (1971), Biondi and Shan (2002), Kaelin and Guitton (2006), and Chattopadhyay and McMechan (2008). The symbol $I(x, z)$ represents the image at (x, z) and \otimes is the cross-correlation. The understanding of cross-correlation has been discussed in section 2.3.1. The zero time-lag assumption reduces the relation to a sum of dot products of two wave-fields in every time sample. This relation also indicates that if these two propagated waves arrive at the same point simultaneously, the scatter can be delineated.

The source wave-field satisfies the equation

$$\nabla^2 p_0(x, z, t) - \frac{1}{c_0^2(x, z)} \frac{\partial^2 p_0(x, z, t)}{\partial t^2} = -\rho(x_s, z_s, t). \quad (2.28)$$

In equation (2.28), the source $\rho(x_s, z_s, t)$, which is specified as a Ricker wavelet in later numerical tests, is consistent with the one used to generate synthetic data. The reference velocity $c_0(x, z)$ is always denoted as the migration velocity model in RTM. The receiver wave-field is a backward propagated wave-field in the migration velocity. In this case, the term $d(x_g, z_g, t)$, which is the data recorded by all the receivers, acts as a time-dependent boundary condition. People usually consider the signals in dataset as "sources" (Baysal et al., 1983). The equation of a 2-D scattered wave-field

is expressed as

$$\nabla^2 p_s(x, z, t) - \frac{1}{c_0^2(x, z)} \frac{\partial^2 p_s(x, z, t)}{\partial t^2} = -d(x_g, z_g, t). \quad (2.29)$$

Consequently, the scattered events in the data are propagated back to the previous positions in reverse-time.

It is necessary to point out that the RTM imaging method is a model-dependent method. The prior required information in RTM are the migration-velocity model, the known source signature, and the dataset. Usually, the source signature and dataset can be controlled, and measured. I want to point out that the migration velocity model needs to be very close to the actual model to generate an encouraging imaging result.

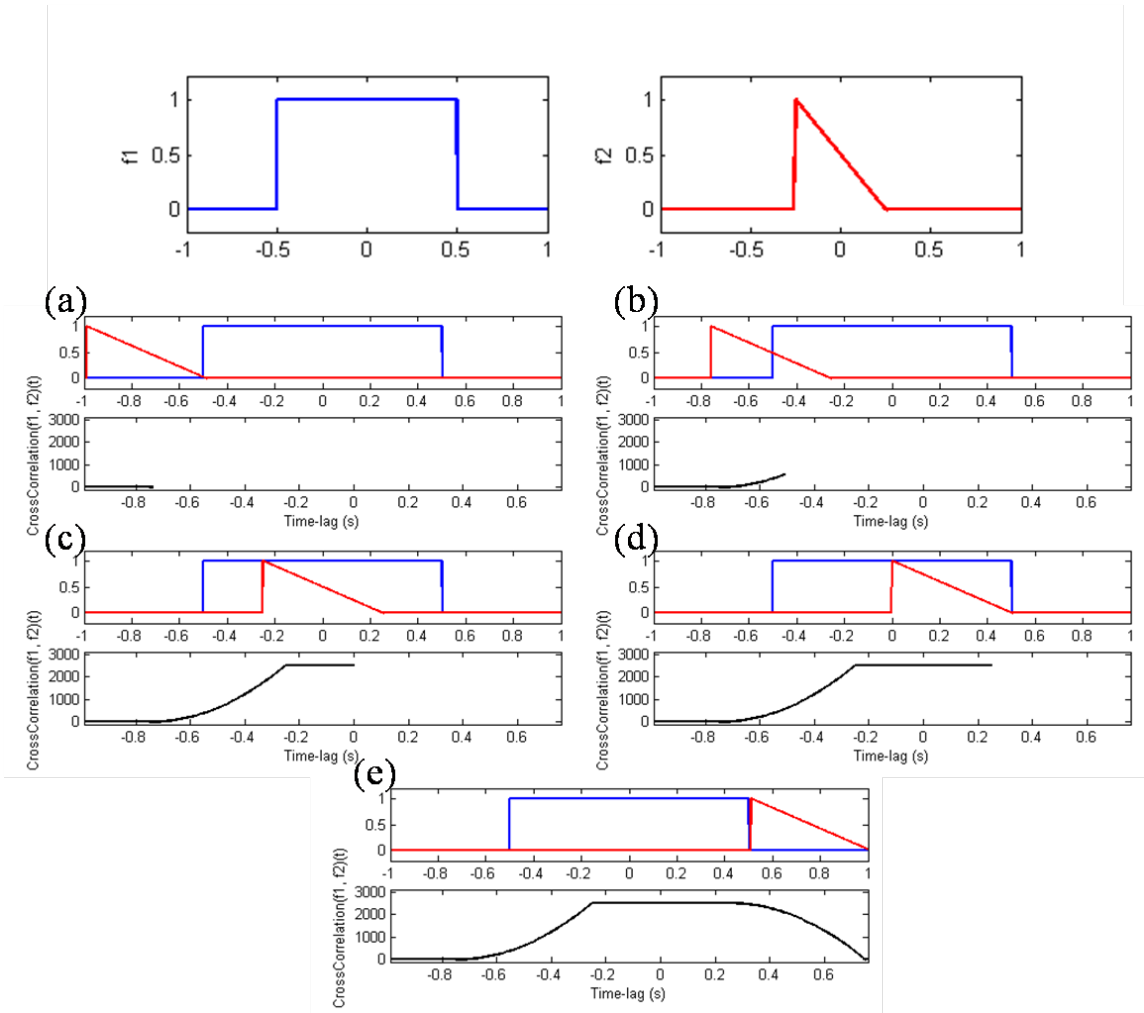


Figure 2.4: One-dimensional cross-correlation example. Top figures plot $f_1(t)$ and $f_2(t)$ varying with time. The $f_2(t)$ (red line) slide from the left to right to cross-correlate $f_1(t)$ (blue line). The time difference caused by the position of $f_2(t)$ is called time-lag. From (a) to (e), the cross-correlation result is assigned on different time-lags. (Courtesy of Reza Arfa)

Chapter 3

Optimal background model extraction

In this chapter, the 1.5-D Born modeling results are shown. When a Born modeling result has a minimum difference with a FD modeling result, which is generated by wave-equation (equation (2.2)) using actual velocities, the background/reference model used in Born modeling is defined as the "optimal background model". In these experiments, the background models are generated by a Gaussian smoothing filter, which considers the $N \times \lambda$ as smoothing length, where N is any rational number and λ represents an average wavelength for a given model and a source signature. The error variances of all tested models are plotted in figure 3.2 and also trace comparisons (figure 3.3) are provided to illustrate the reason of the different error variances.

3.1 Modeling methods

The definitions of the Born modeling result and normal FD result should be clarified at first. Equation (2.18) can generate one shot gather using FD scheme, which is defined as Born modeling result. With the same source location, the normal FD result is generated by the wave-equation

$$\nabla^2 P(x, z, t) - \frac{1}{c^2(x, z)} \frac{\partial^2 P(x, z, t)}{\partial t^2} = -\rho(x_s, z_s, t), \quad (3.1)$$

using the actual velocities $c(x, z)$.

The comparison of Born modeling results and normal FD results are investigated from two perspectives.

One perspective is the curve diagram plotted by the error variances of results generated using two methods, as shown in Figure 3.2. There are seven sub-figures in this group. Every sub-figure uses the multiple N as horizontal axis and variance error as vertical axis. If there are two matrix as \mathbf{d}_1 and \mathbf{d}_2 whose size are both $n \times m$, then the variance error between them is

$$Error(\%) = \sum_{i=0}^n \sum_{j=0}^m \frac{(d_1(i, j) - d_2(i, j))^2}{n \cdot m}, \quad (3.2)$$

where i and j are the indexes for obtaining the elements in the matrix. In these experiments, \mathbf{d}_1 and \mathbf{d}_2 are specified as data generated by normal FD modeling and Born modeling. In addition, the experiments are taken at several discrete points, which are shown as * in diagrams. In order to find a minimum variance, the sampling sites are set more intensely in the likeliest range. The results indicate that in each sub-figure, there is a minimum point of error variance which I describe as an "optimal"

point. Every optimal point corresponds to an optimal smoothing length (on the horizontal axis). If Born modeling uses the background model smoothed by the optimal smoothing length, the data generated by Born modeling is the closest to the normal FD result, which is considered as the actual result. Even though the optimal points for different model are not located at a fixed value, the regularity still can be obtain.

The other approach is trace comparisons, which are plotted to find the origins of different variance errors. The wiggle comparisons at 500m offset trace are shown in of figure 3.3. In each plot, the vertical axis not only represents the amplitude but also is denoted by the different smoothed length used for comparisons. In each trace pair in the comparisons, the red and blue traces are generated by normal FD and Born modeling, respectively.

3.2 Modeling parameters

Seven different models of the same size are tested (900×600 grids, $10m/grid$). Five of them are two-layer acoustic mediums with only one reflector at $2500m$ depth. The controlled contrasts of the models range from $2000m/s$ versus $2100m/s$ (weak contrast) to $2000m/s$ versus $5000m/s$ (strong contrast) as shown in Figure 3.1(a).

In addition, a multiple layer model and a well-logging model are tested. The multiple layer model (Figure 3.1(b)) is created by gradually increasing velocities from top to bottom, which range from $1700m/s$ to $2500m/s$. The last model is extracted from a real sonic velocity well-log. The aim of this project is modeling scattered waves so

that constant layers are extended to the top and bottom to easily clip reference waves out, as shown in Figure 3.1(c). Monitoring time of wave-propagation is 5 seconds in numerical tests and dominant frequency of the Ricker source is set as $15Hz$. Since the models are in 1-D variance and the source is a 2-D line source, the modeling is performed in 1.5-D.

3.3 Tests of two-layer models

To unveil the regularity of selecting an optimal background, I generated the simplest two-layer models using different velocity contrasts as $2100m/s$ versus $2100m/s$, $2500m/s$, $3000m/s$, $4000m/s$, and $5000m/s$, respectively.

From the error curves of two-layer models (figure 3.2(a)-3.2(e)), the "optimal" point shifts from 0.5λ to 1.5λ point as the velocity contrast increases. I find that an interesting phenomenon occurs around the error point given by Born modeling using 0.5λ as the smoothing length. The "optimal" point is never located under this 0.5λ smoothing length but tends toward it even if there is a large contrast in the model (Figure 3.2(e)).

The trace comparisons in figures 3.3(a) to 3.3(c) demonstrate that the amplitude of a wavelet is uncompensated when the background model is smoothed by a small length, which cannot produce enough perturbation to reconstruct a reflection. However, the phase of a wavelet shifts when the background is severely smoothed, usually over 1.5λ . Over-smoothing is associated with a large perturbation. In addition, the reconstruction of Born modeling behaves much worse when the contrast is large

enough (figure 3.3(c)) to violate the small contrast assumption of the Born approximation.

Let us take a look into the reasons of these phenomena. The trace comparisons are only performed on scattered waves, which assumes that there is no reflection in the reference wave-field, but the numerical smoothed models cannot guarantee this assumption. When the reference model is generated by less than 0.5λ Gaussian smoothing, the contrasts in reference still produces reflections. The summation of p_0 and p_s remains (equation (2.15)). Consequently, the residue of scattered waves in the reference wave-field decreases the scattered energy in the Born modeling result. This is why the amplitude cannot be recovered in Born modeling using slightly smoothed reference. On the other hand, when the reference is smoothed severely by over 1.5λ , the root-mean-square (RMS) velocity above the reflector is changed. The travel time of reflected events only corresponds to the velocity above the reflector. This intuitive way can explain the phase shift in the trace comparison.

More results of complicated models are presented in section 3.4 to verify the regularity and examine the rough background model prediction from two-layer model tests.

3.4 Tests of well-logging model and multiple layer model

In this section, two complicated models are tested for a further understanding of the optimal background velocity selectivity. The problem is explored using the same approaches as described in section 3.2. Also, the rough estimates of optimal points are made with the help of previous two-layer models tests.

A multiply layer model (Figure 3.1(b)) is tested for Born modeling, using $1700m/s$, $1800m/s$, $2000m/s$, $2350m/s$, and $2500m/s$ as velocities in each layer, respectively. The variance error for the multiply layer model is plotted in figure 3.2(f). From this figure, the error point located at 1.0λ can be acquired as the optimal point. Compared with the results of two-layer model tests (figure 3.2(a)-3.2(e)), the optimal smoothing length of the multiple layer model is an intermediate value between optimal smoothing lengths of $2000m/s$ vs. $2100m/s$ model and $2000m/s$ vs. $2500m/s$ model (Figure 3.2(a) 3.2(b)). The rough estimation depends on the maximum velocity contrast in the model. Moreover, as the two-layer model tests show, when smoothing before the optimal point, the distortion of amplitudes dominantly contributes to the error variance, while phase shifting becomes the leading cause of the large error variance when the model is smoothed over the optimal point (figure 3.3(d)).

Furthermore, the synthetic well-logging model is established by log velocities in depths from $1400m$ to $4500m$. The well-logging model is extended to the surface and bottom with constant velocities (figure 3.1(c)). The error variance curve (figure

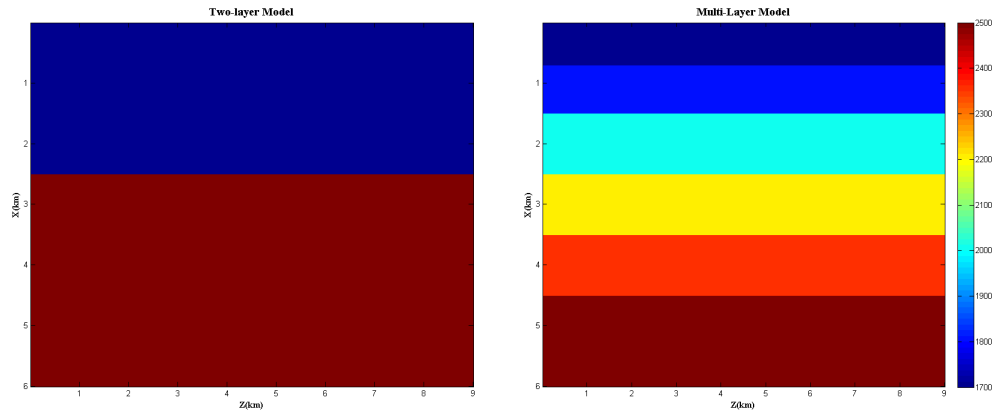
3.2(g)) shows that 0.6λ is the optimal smoothing length to generate a well-logging background model. If the rough Gaussian smoothing length of a well-logging model is needed, it can be approximately estimated by figure 3.2(d), according to the maximum contrast exhibited in figure 3.4.

3.5 Conclusions

This chapter provides the parameters and the results of numerical tests for extracting an optimal background/reference model used in Born modeling. If there is a criterion of selecting the reference, the optimal background model used in Born modeling can be roughly estimated for a given model. The 1.5-D Born modeling results provide a criterion of selecting an optimal Gaussian smoothing length.

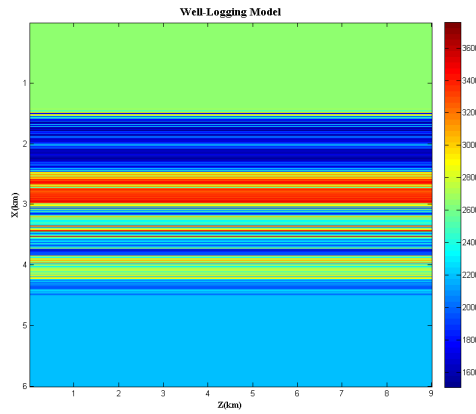
Please note that Born modeling cannot be expected to reconstruct an accurate phase and amplitude of events because Born approximation considers linear scattering in wave-propagation. This approximate modeling works only if there is a small contrast in the model and a small aperture in the dataset, which is described in section 2.2.2. The minimum error points shown in figure 3.2 indicates that the range of optimal smoothing length is very limited, from 0.5λ to 1.5λ . Figure 3.3 illustrate that when the reference model is smoothed by a length less than 0.5λ , the Born results fail to recover the amplitude of wavelets. This is because reflections still exist in reference wave-fields, which cut down the scattered energy in Born modeling results (equation (2.15)). The criterion of selecting a reference model is that the effective Gaussian smoothing length is from 0.5λ to 1.5λ for Born modeling.

From the investigations of the reference model, the quality of a Born modeling result can be controlled. But what is the importance of Born modeling and how does it apply to other processing steps, like imaging? In the next chapter, an algorithm based on Born modeling to improve imaging illumination is proposed and a sub-salt model is tested for verifying the effects. As an upper limit in Born modeling, 1.5λ Gaussian smoothing length will be used to generate a background/reference model in imaging tests.



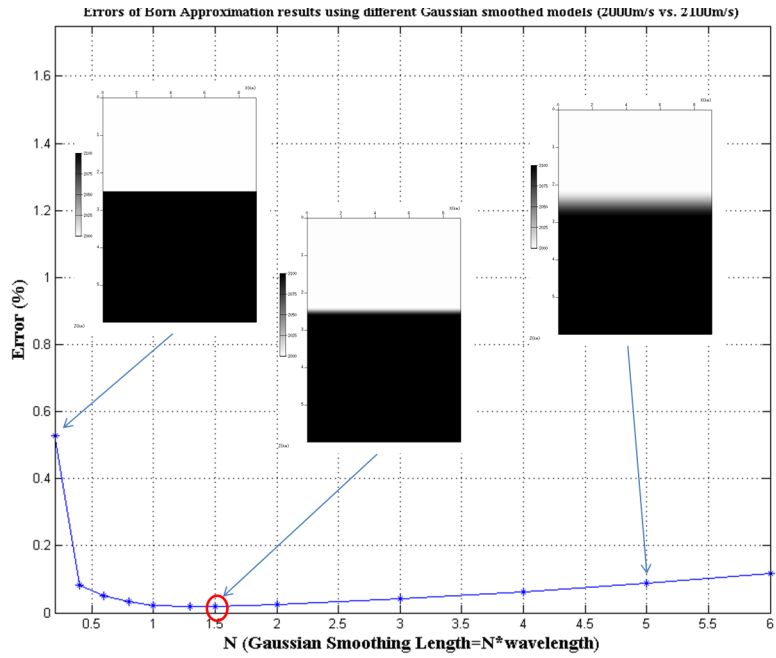
(a) Two-layer model

(b) Multi-layer model

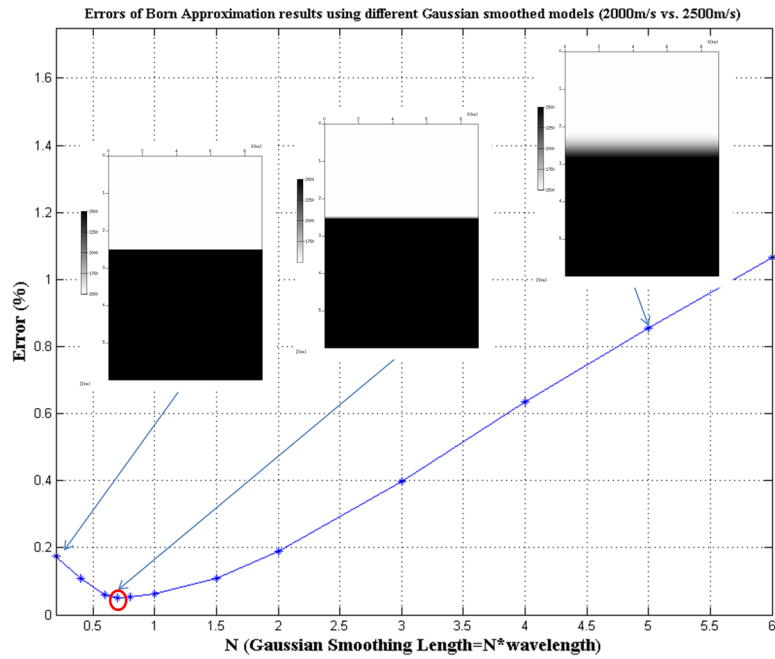


(c) Well-logging model

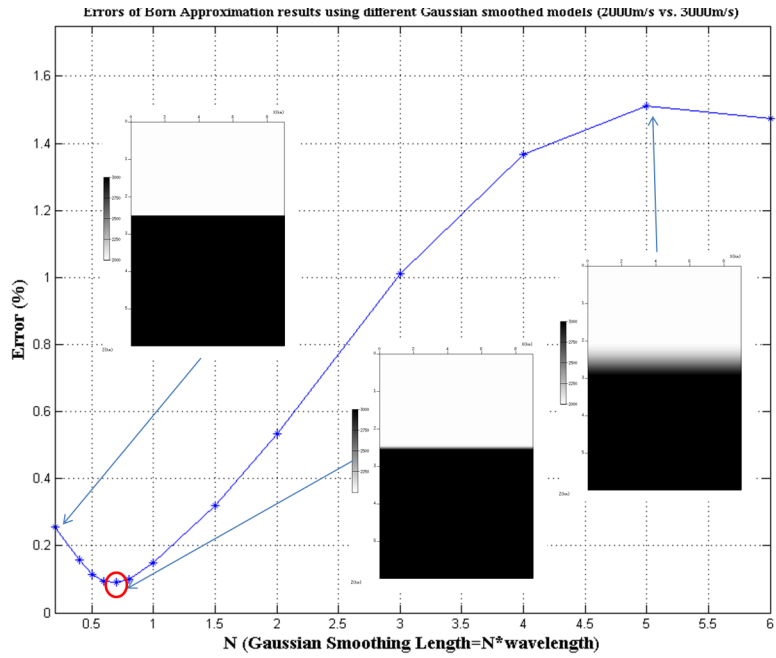
Figure 3.1: Different acoustic models using in experiments



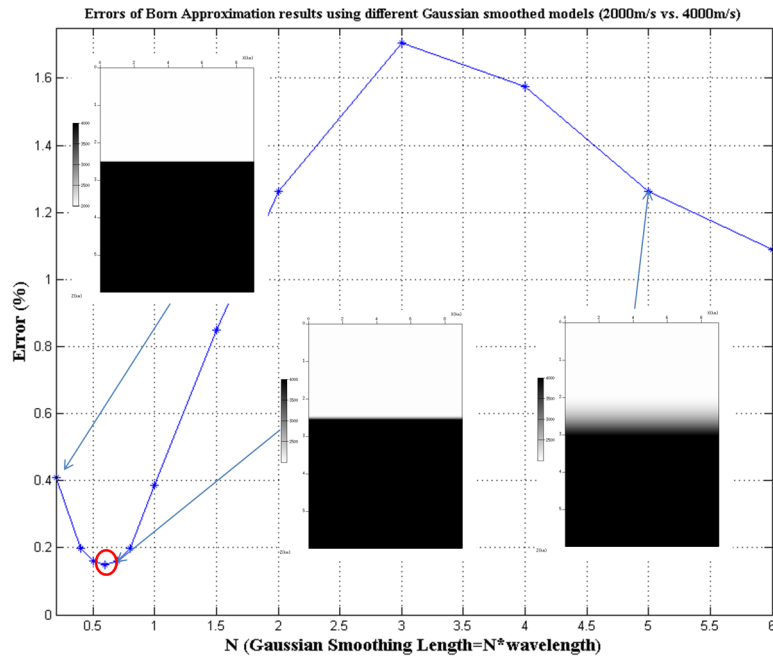
(a) 2000m/s vs. 2100m/s model



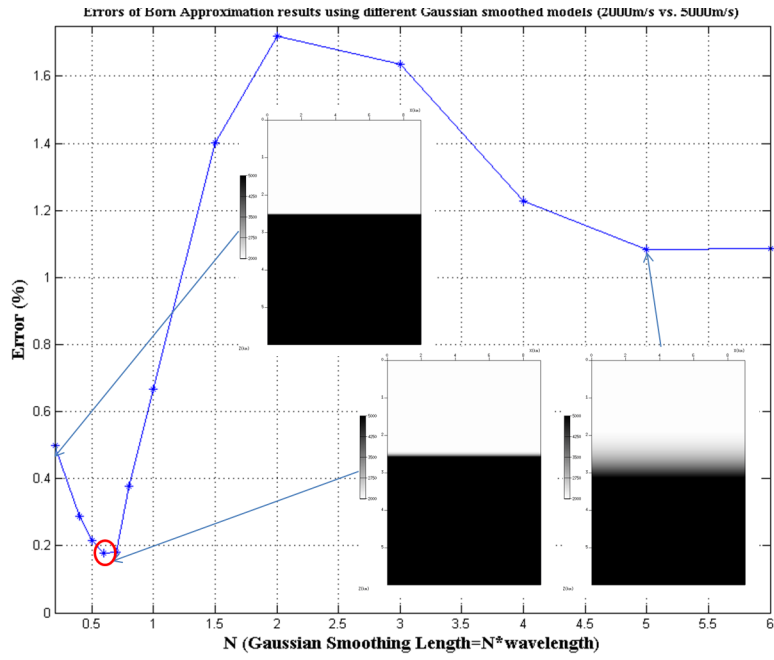
(b) 2000m/s vs. 2500m/s model



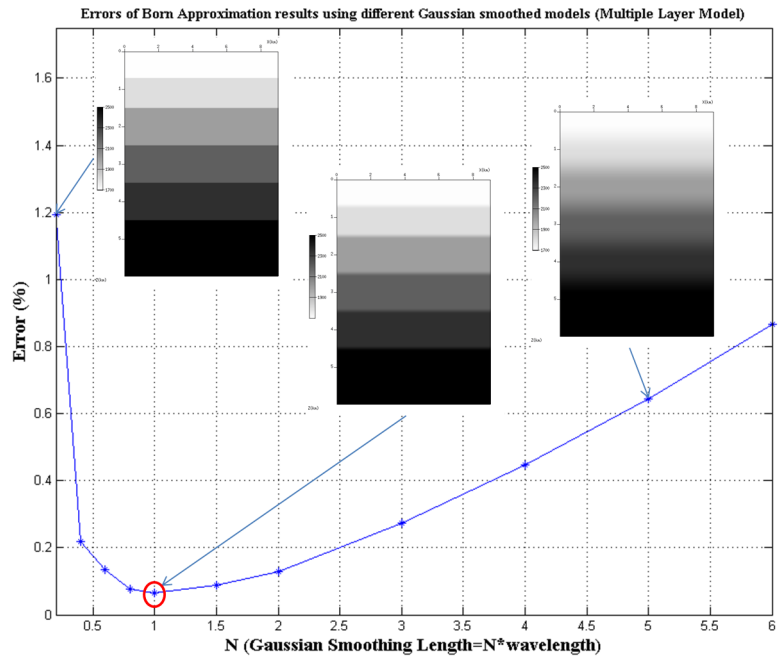
(c) 2000m/s vs. 3000m/s model



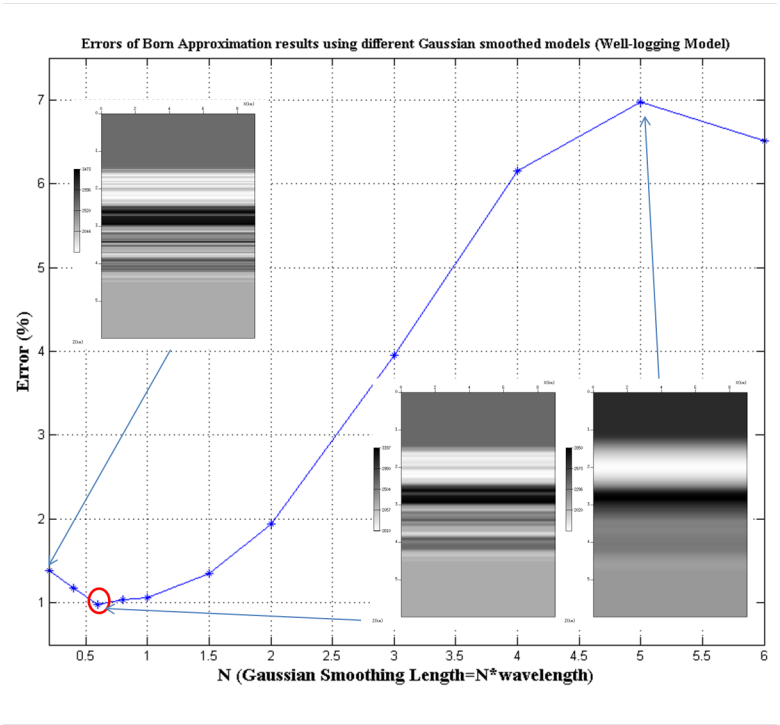
(d) 2000m/s vs. 4000m/s model



(e) 2000m/s vs. 5000m/s model

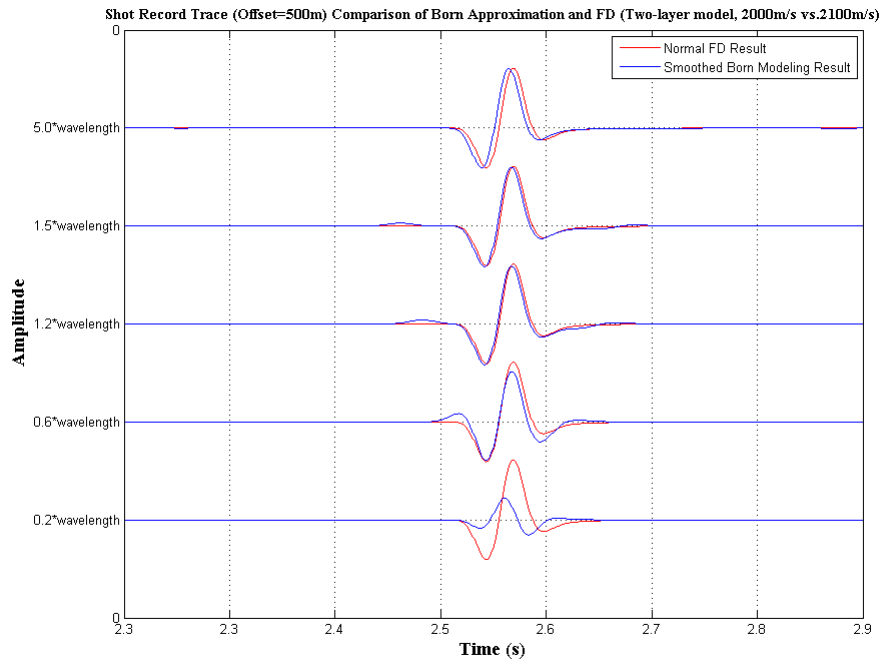


(f) Multiple layer model

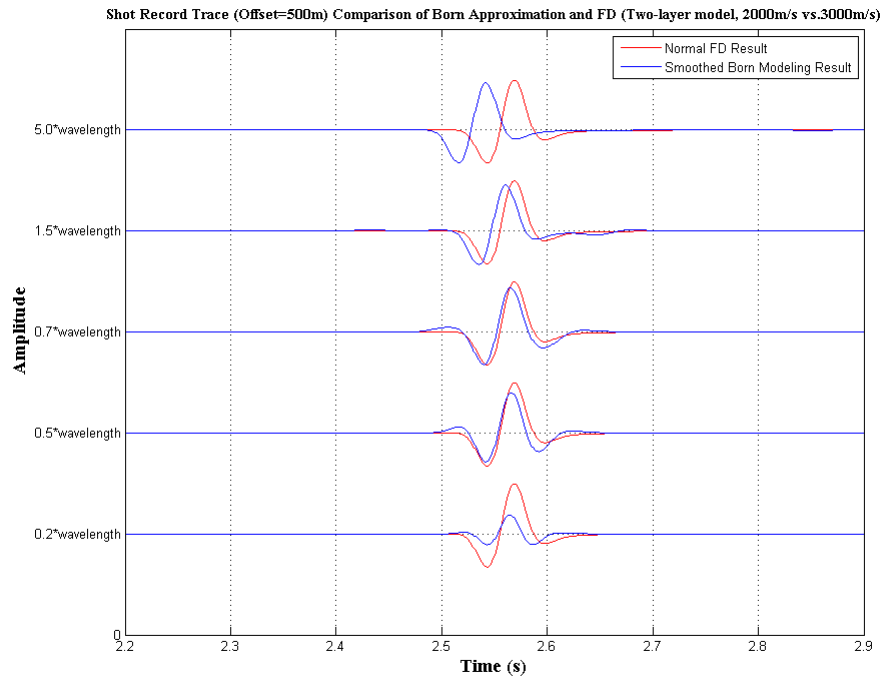


(g) Well-logging model

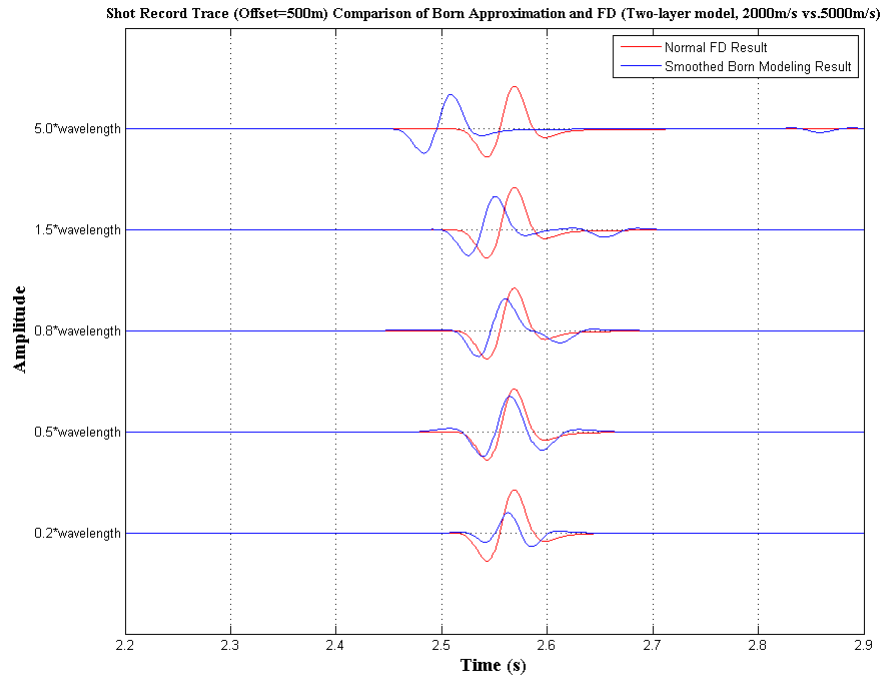
Figure 3.2: Error variance between Born modeling and normal finite-difference data. In each diagram, the star points (*) represent the error variances calculated by an unified FD result and various Born modeling results using different background models and the red circle denotes the optimal smoothing point. The background models are generated by the Gaussian smoothing of actual models using different smoothing length ($N \times \lambda$). The background/reference models smoothed by 0.2λ , optimal length and 5.0λ are shown in each diagram.



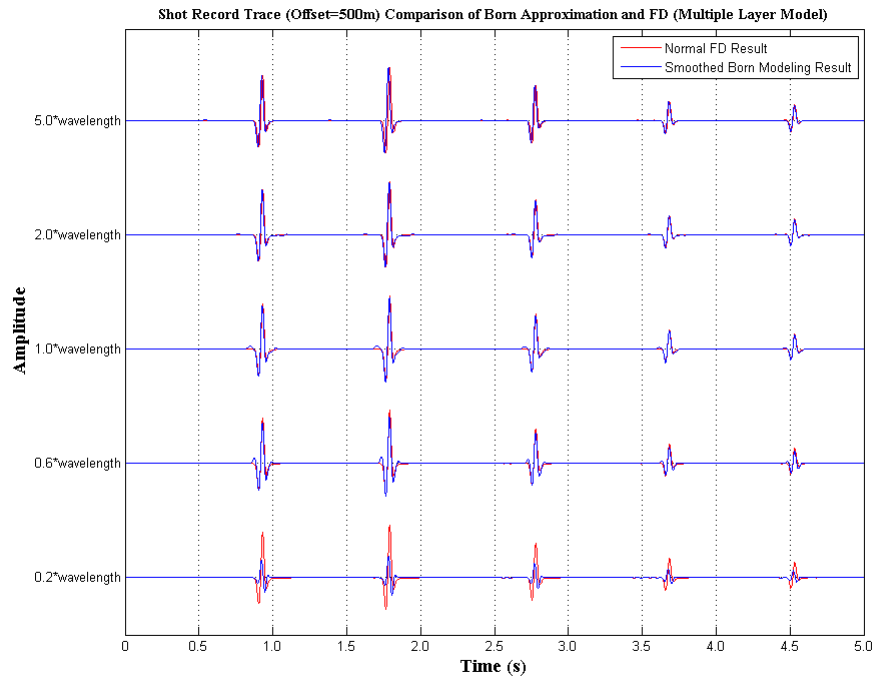
(a) 2000m/s vs. 2100m/s model Born result trace



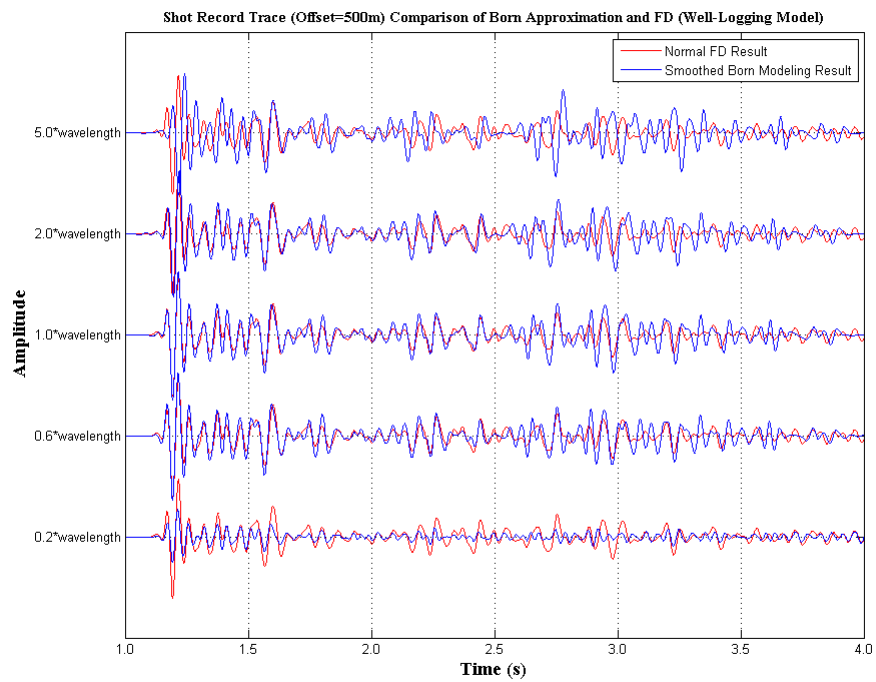
(b) 2000m/s vs. 3000m/s model Born result trace



(c) 2000m/s vs. 5000m/s model Born result trace



(d) Multiple layer model Born result trace



(e) Well-logging model Born result trace

Figure 3.3: Trace comparison between Born modeling and normal finite-difference data. The trace channel located at 500m offset. The background models are models Gaussian smoothed by a multiple (N) of λ .

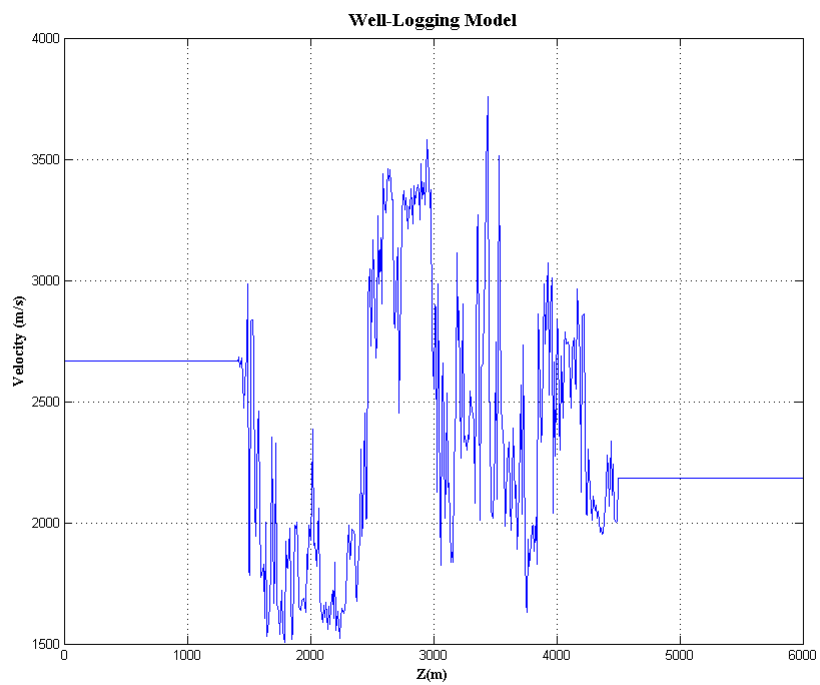


Figure 3.4: Synthetic well-logging velocity model.

Chapter 4

Improvement of reverse-time migration (RTM) illumination

In this chapter, I will introduce an improved RTM method based on Born modeling. As discussed in chapter 1, original RTM fails to image structures beneath a sub-salt body with low illumination, which is called the "sub-salt problem". The origins of this problem are briefly reviewed at the beginning in section 4.1. Such problems generated significant interest in seismic studies. In section 4.2, extending the studies in Fleury and Vasconcelos (2010), I present an improved RTM using perturbed wavefields and cross-correlation imaging condition. In section 4.3 I will examine both original and improved RTM with a sub-salt model. These results help us understand the values and defects of improved RTM compared to original RTM.

4.1 Sub-salt problem

The sub-salt problem has been recognized from imaging work in the extensional Gulf of Mexico in the last decades (O'Brien and Gray, 1996; Rosenberg, 2000). If salt or other high-velocity layer exists in sediment layers, the seismic ray path can be severely distorted because of the high acoustic impedance contrast. In this case, the salt bodies can be considered as sonic lenses, which focus the rays. Besides, the high impedance prevents most of the incidence energy associated with total reflections at relative large incidence from penetrating, so that less wave energy can travel to the area beneath the salt body. Both reasons can result in the low illumination under a salt body, where the area is named "shadow zone". Here, let us explain details in how the salt body blocks the waves as lenses by studying the literature.

To find out the paths of wave propagation, many researchers use ray-tracing modeling to plot common reflection gathers (CRP) (Muerdter et al., 2001). In this kind of result, the ray paths are shown from source to a same reflection point. Here, I provide a schematic in figure 4.1 to illustrate ray-tracing and how wave paths are distorted by a high impedance dipping layer. As mentioned above, the salt layer acts as a focus lens to concentrate the signals to a small area. The primaries in data can illuminate some of the structures, like the red point in figure 4.1. However, because of the beam concentration, few primaries signals in data comes back from the "shadow zone". This part of the structure faces the issue to be reconstructed in depth imaging, such as RTM and Kirchhoff migration. If you are interested in more knowledge of ray-tracing methods and relations between reflection angle, salt thickness, and salt dipping angle, please refer to Muerdter et al. (1998), Muerdter

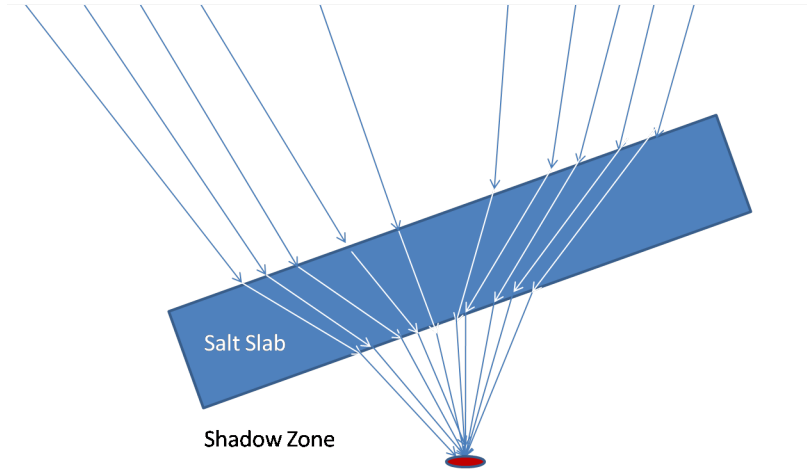


Figure 4.1: Schematic for a ray-tracing result of a salt slab

et al. (2001).

The difficulties of detecting structure under salt and interpreting reservoir locations promote the development of conventional migration methods. In the next section, a revised algorithm will be presented, which is based on RTM and Born modeling. Instead of utilizing primaries alone, this method attempt to use the information in multiples to illuminate the "shadow zone".

4.2 Algorithm based on Born modeling

Original RTM imaging can provide encouraging imaging results when dealing with complex geological structures. However, the low illumination is a problem when a sub-salt body or other high velocity layer exists. As mentioned in section 4.1, the high velocity structure blocks the structures beneath and generates a "shadow zone",

because the original RTM assumes that pre-processed primaries, which means only primaries touching zones can be imaged in principle. That is also why researchers are dedicated to getting rid of noise, like de-ghosting and multiple removal (Araújo et al., 1994; Weglein et al., 2002; Zhang and Weglein, 2005). In this section, motivated by the sub-salt problem, I propose a Born modeling-based method to generate wave-fields in RTM, enlightened by the researches of Fleury and Vasconcelos (2010) and Fleury and Snieder (2011). In this work, I make an attempt of using the scattered wave-field to image. This is an initial and elementary step towards the future work on solving "shadow zone" problem. Progress is going to be made, but the initial step is always worthwhile.

The input for this improved algorithm should be clarified in advance. Velocity analysis and linear inversion work are assumed to be done before imaging, in order to have a background/reference model and an estimated perturbation $\alpha(x, z)$. The linear and non-linear perturbation construction can be reviewed Weglein et al. (2003) using inverse scattering series. This inversion work is important for imaging and interpretation but will not be discussed here. Since the tests are performed on a synthetic model, the perturbation can be obtained by relation in equation (2.11).

The formula introducing Born modeling into the propagation of wave-field can be expressed as,

$$\nabla^2 p'_0 - \frac{1}{c_0^2(x, z)} \frac{\partial^2 p'_0}{\partial t^2} = -\alpha(x, z) \frac{\partial^2 p_0}{\partial t^2}, \quad (4.1)$$

$$\nabla^2 p'_s - \frac{1}{c_0^2(x, z)} \frac{\partial^2 p'_s}{\partial t^2} = -\alpha(x, z) \frac{\partial^2 p_s}{\partial t^2}, \quad (4.2)$$

where p_0 and p_s are the source wave-field and the receiver wave-field as described in equations (2.28) and (2.29). Compared with the wave-propagation idea in original

RTM, the new method adds linear scattering into the source- and receiver-field instead of assuming non-reflection in the wave-field. The imaging condition for RTM scheme remains and the new imaging result noted as I' in,

$$I'(x, z) = \sum_{sources} p'_0(x, z, t) \otimes p'_s(x, z, t). \quad (4.3)$$

The revised imaging result contains the quadratic scattering information. In original RTM, the imaging points are the cross-correlation of two down-going waves at zero time-lag (figure 4.2(a)), which means using primaries. Nevertheless, the improved RTM tries to map a point using two up-going waves (figure 4.2(b)). The prior information for the improved RTM are a source signature, a reference model and a(n) (estimated) perturbation term (equations (4.1),(4.2)). A true perturbation defined by equation (2.11) is assume to be known in later tests in order to simply test the migration algorithm. In addition, the FD scheme is applied in numerical testing on RTM scheme.

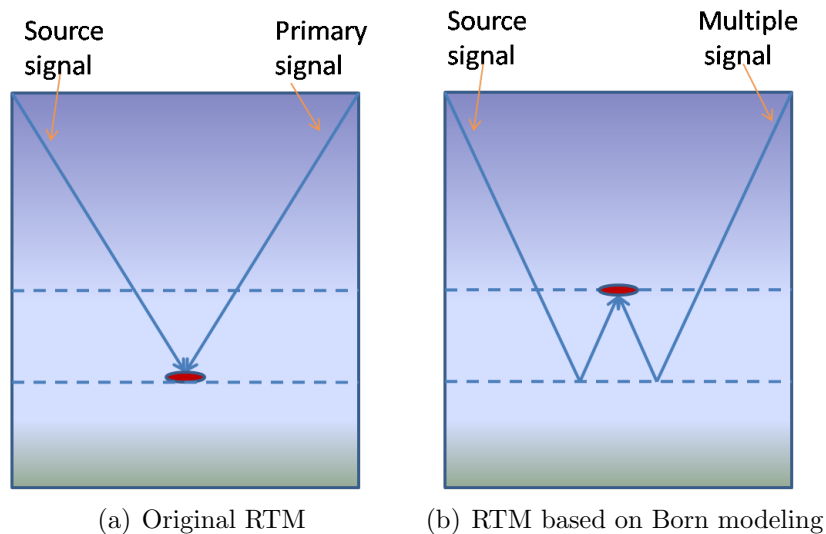


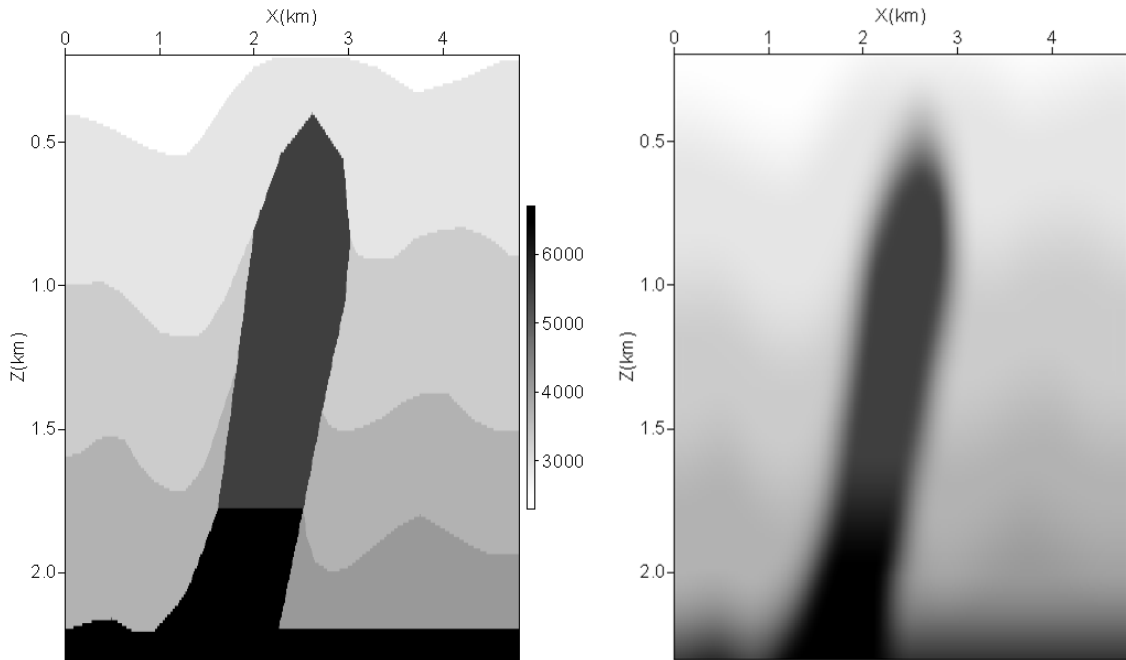
Figure 4.2: Imaging principle diagram of original RTM and Born modeling based RTM

4.3 Salt model tests

A sub-salt model, as shown in figure 4.3(a), is used in the final tests of both original and improved RTM. The velocities vary from $2500m/s$ to $6500m/s$. For migration purposes, the background model is a Gaussian smoothed actual model by 1.5λ (figure 4.3(b)). FD scheme is used for implementation.

The original RTM result of the sub-salt model is shown in figure 4.4(b), compared with the actual model. The implementation is based on equation (2.27), (2.28) and (2.29). The result in figure 4.4(b) reaches its target of imaging the sedimentary layers using the primaries information. But the salt flank on the right side in the "shadow zone" and the connections between salt-body and sedimentary layers can be barely seen. This low-illumination phenomena is aroused by ignoring multiply scattered waves information, as well as the limited source aperture. From deep

depths imaging, the pseudo-reflectors appear at the bottom of salt-body, which leads to difficulty of interpreting. Most of the leg-like artifacts correspond to the limitation of the acquisition aperture.

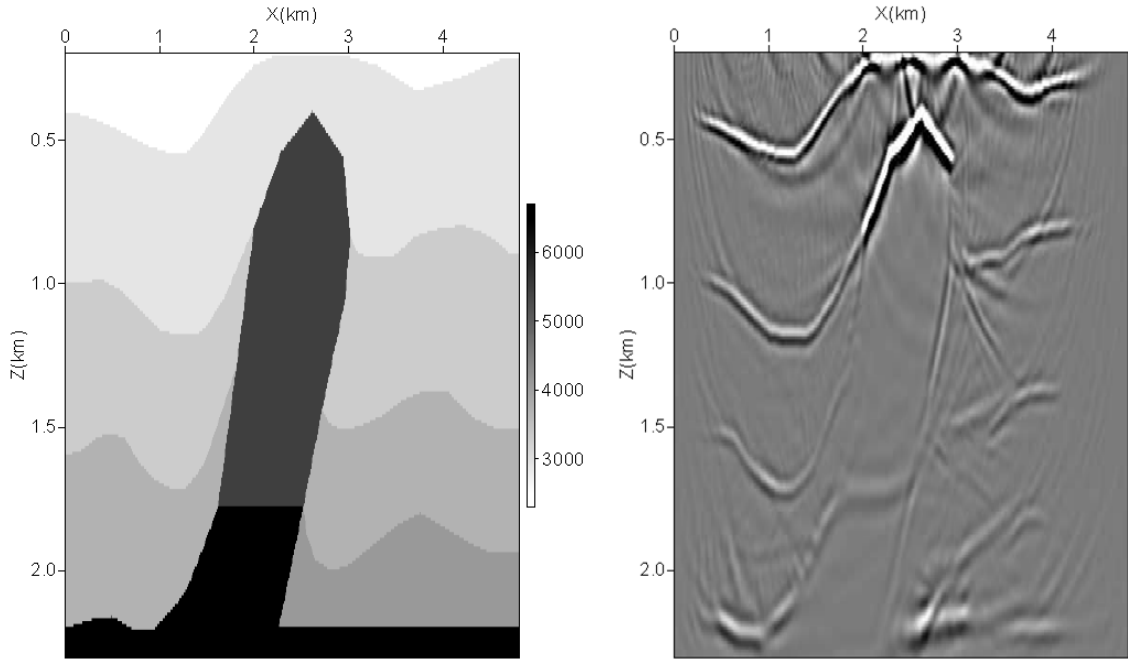


(a) Salt model

(b) Smoothed salt model

Figure 4.3: Original salt model (courtesy of Allied Geophysical Laboratory) and smoothed salt model

The improved RTM result in figure 4.5(b) is provided to investigate if it can delineate the structure detail missing in the original RTM result. The implementation is based on the proposed equations (4.1), (4.2), and (4.3). From RTM result in figure 4.5(b), the two connections on right salt flank are reconstructed by migrating multiples. But the bottom structure errors grow worse. In principle, on the condition that both



(a) Salt model

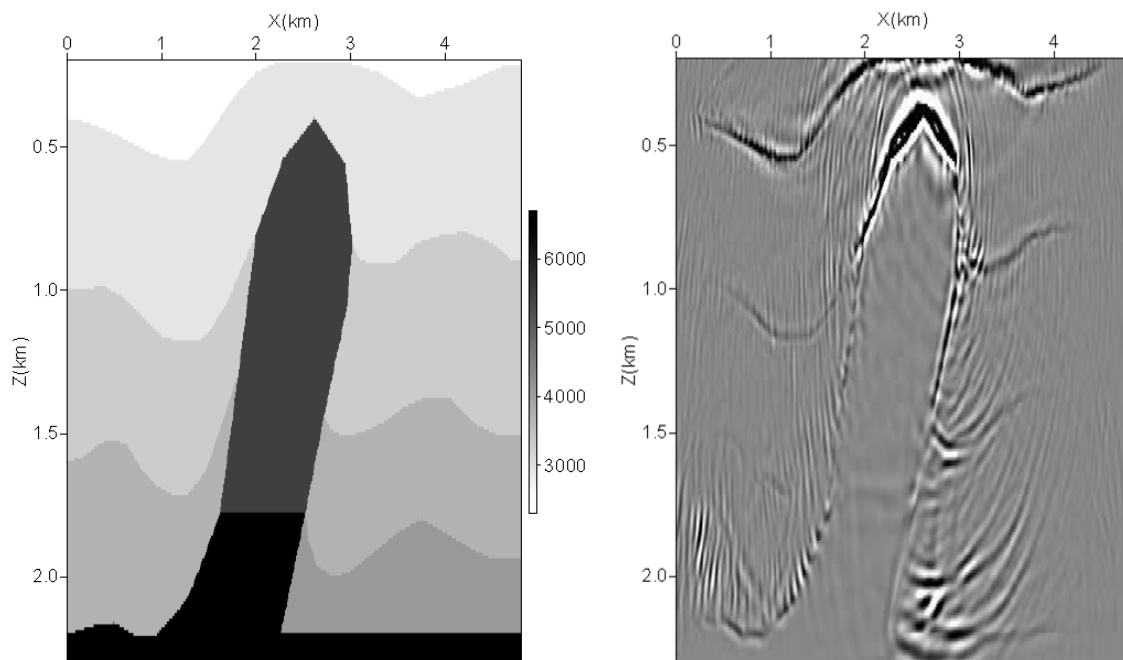
(b) Original RTM result

Figure 4.4: Original reverse-time migration result

the forward and backward wave-fields are linearly scattered by Born modeling, the result can emphasize the structures which generate the downward reflections (figure 4.2(b)). However, it fails to image the structure in deep depths. That is because all the events in the data get involved in backward propagation. The complex multiply scattered events, like higher order multiples, cannot be recovered to its actual travel-time or depth location in reverse-time by scattered only once. The signals of higher order multiples arrive later (larger travel-time) in the recorded data, than first-order multiples and primaries. If this issue happens, a higher-order multiple considers itself

as a first-order multiple, which is generated by a false deeper depth reflector.

Finally, the RTM on basis of Born modeling indeed utilizes the multiples with the evidence of rebuilding the salt-sediments connections and the salt flank boundary in the "shadow zone". The combination of results in figure (4.4(b)) and figure (4.5(b)) can help later interpretation work.



(a) Salt model

(b) RTM on basis of Born modeling

Figure 4.5: Reverse-time migration result on the basis of Born modeling

4.4 Conclusions

Section 4.1 states "sub-salt problem" in detail. In this section, I review Muerdter's work (Muerdter et al., 1998; Muerdter et al., 2001) on detecting the low-illumination zone by ray-tracing method. The high-velocity property of salt generates a high acoustic impedance between salt-body and sedimentary layers. This kind of high impedance makes the salt-body play a role as concentration lens, which focus wave beams. The areas that cannot be touched by primaries are called "shadow zones". The following section 4.2 presents the key work in this thesis - an improved RTM which introduces the perturbed wave-fields into RTM scheme. To examine the effects of different algorithms, numerical tests of original and improved RTM on the same sub-salt model are presented in section 4.3. I have to point out that the prerequisite of using the improved RTM, is obtaining an estimated perturbation in practical work. In this thesis project, the difference between actual and background model is treated as a perturbation, which is a true perturbation. This seems like a redundancy between perfect inversion and improved imaging. However, to simply test the migration algorithm, I use the true perturbation, avoiding the inversion procedure. From the numerical result in figure 4.4(b), the original RTM indeed produces low illumination imaging of the structures hidden by salt. For instance, the sub-salt flank and connections between salt and sedimentary layers can be barely seen in this result. This issue promotes the development of migrating multiples. Another imaging result (figure 4.5(b)) improved by Born modeling is expected to enhance the imaging illumination under salt-body. The figure proves the capability of the improved RTM, which can delineate the connection points and map salt boundary in shallow depth.

However, linear perturbed wave-fields cannot recover the depth information of higher-order multiples in migration, so that complex events are perturbed in wrong locations and this situation causes pseudo-reflectors. That is also why there is a mess after using perturbed wave-fields in deep depths imaging, where higher-order multiples are wrongly located. In addition, both these migration methods suffer from serious artifacts of aperture limitations.

Even though there are issues in the improved RTM results, this method still shows its potential on migrating multiples, which maps the detailed structures on salt-flank and provides valuable information for later geological interpretations.

Chapter 5

Summary

Current Born modeling work requires prior information, such as a reference medium and an estimated perturbation. Also, the widely used reverse-time migration is a model-dependent method. However, studies of this reference model are rarely conducted. Another issue stated in this thesis is that RTM can handle most of the imaging of geologic structures unless sub-salt bodies or high-velocity layers exist in the subsurface. Sub-salt structures focus the wave beams from the view of ray theory and prevent the primaries from touching some areas, which leads to a failure in imaging beneath the high-velocity structures low illumination. This thesis mainly discusses the properties of Born modeling from extracting an optimal background/reference model and the application of Born modeling for improving the RTM illumination. The full thesis can be divided into four parts. Chapter 1 reviews the history of using background models starting from inversion and states that the advantage of a smoothed background model can be utilized in Born modeling and RTM scheme.

The key concept of Born approximation and the numerical implementation in tests are reviewed in detail in chapter 2. Selecting an optimal background/reference model is found by testing different layered models in chapter 3. Chapter 4 shows the migration results using both original and the improved RTM schemes. The thought behind the later imaging tests is to utilize the energy of multi-scattered waves, which are ignored and assumed to be removed in industry standard original RTM.

In chapter 3, compared with the normal FD data, which is generated by FD modeling wave-equation using actual velocity, the Born modeling can approximately forward model the primaries in dataset. It fails to reconstruct the amplitudes of events when the reference model is Gaussian smoothed by less 0.5λ , because the reflections still exist in reference wave-field. λ here is an averaged wavelet for a given model and a source signature. On the other hand, when the background model is far from the actual model, the phase of the wavelets shifts due to the severe change of velocities above the reflector. In this thesis, the criterion of generating a background model or determining a perturbation is characterized by Gaussian smoother length. Through the numerical tests of various models, the maximum value of error variance between a normal FD result and a Born modeling result is around seven percent, as shown in figure 3.2(g). The optimal smoothing length remains in a stable range from 0.5λ to 1.5λ . This regularity can be applied in Born modeling or migration work which requires the reference model as input.

In chapter 4, original reverse-time migration faces the imaging problems of unclear salt boundary and salt-sediments under a high-velocity salt structure (figure 4.4(b)). The area which primaries do not touch can be described as a "shadow zone" with low

illumination. The issue of sub-salt imaging promotes the development of migrating multiply scattered waves.

Since an improved RTM is expected to enhance the imaging illumination under a salt-body, I introduce the scattering into source and receiver wave-fields, which are defined in original RTM, by applying Born modeling. The result indeed delineates the connection points and salt boundary for considering the energy and information in multiply scattered waves (figure 4.5(b)), so that the multi-scattered energy, which is usually ignored, can be preserved. However, the deep structures failed to be correctly mapped, because the complex events cannot be recovered in the history of propagation by adding only a linear perturbation. Also, migration methods suffer from serious artifacts due to aperture limitations and two-way wave-fields in the space-and-time domain.

Other advanced work should be done. For example, the imaging condition can be altered by other non-linear relations in the literature (Fleury and Vasconcelos, 2010). Some more advanced technologies are free of the migration background model, like ISS imaging using inverse scattering series, which is being comprehensively studied and implemented (Shaw and Weglein, 2003; Liu et al., 2005).

Appendix A

Fourth-order accuracy FD scheme example

In this case, the Taylor expansions involving four nearby discrete points can be expressed as,

$$\begin{aligned} P(x - 2\Delta x) &= \\ P(x) - \Delta x P'(x) + \frac{(2\Delta x)^2}{2!} P''(x) - \frac{(2\Delta x)^3}{3!} P'''(x) + \frac{(2\Delta x)^4}{4!} P''''(x) - \mathcal{O}(\Delta x^5), \\ P(x + 2\Delta x) &= \\ P(x) + \Delta x P'(x) + \frac{(2\Delta x)^2}{2!} P''(x) + \frac{(2\Delta x)^3}{3!} P'''(x) + \frac{(2\Delta x)^4}{4!} P''''(x) + \mathcal{O}(\Delta x^5), \\ P(x - \Delta x) &= \\ P(x) - \Delta x P'(x) + \frac{\Delta x^2}{2!} P''(x) - \frac{\Delta x^3}{3!} P'''(x) + \frac{\Delta x^4}{4!} P''''(x) - \mathcal{O}(\Delta x^5), \\ P(x + \Delta x) &= \\ P(x) + \Delta x P'(x) + \frac{\Delta x^2}{2!} P''(x) + \frac{\Delta x^3}{3!} P'''(x) + \frac{\Delta x^4}{4!} P''''(x) + \mathcal{O}(\Delta x^5). \end{aligned} \quad (\text{A.1})$$

Taking some algebraic steps on equation (A.1) to get rid of $P'(x)$, $P'''(x)$ and $P''''(x)$. The summation of $P(x + \Delta x)$ and $P(x - \Delta x)$ can cancel out the odd terms in series, so does the summation of $P(x + 2\Delta x)$ and $P(x - 2\Delta x)$. The result of $P''(x)$ turns to be,

$$P''(x) = \frac{-\frac{1}{12}P(x - 2\Delta x) + \frac{4}{3}P(x - \Delta x) - \frac{5}{2}P(x) + \frac{4}{3}P(x + \Delta x) - \frac{1}{12}P(x + 2\Delta x)}{(\Delta x)^2} \quad (\text{A.2})$$

Appendix B

Born modeling in space-and-time domain

Starting from the Born series, the Born modeling term can be explicitly expressed in frequency domain using the Green's function in reference medium and the perturbation term (Weglein et al., 2003). To describe a wave propagation in medium, let

$$\mathbf{L}G = -\delta(\mathbf{r} - \mathbf{r}_s), \quad (\text{B.1})$$

where \mathbf{L} is the actual differential operator and G is the matrix elements of actual Green's operator. After using the scattering theory, the reference differential operator (\mathbf{L}_0) and matrix elements of reference Green's operator (G_0) satisfy the equation,

$$\mathbf{L}_0G_0 = -\delta(\mathbf{r} - \mathbf{r}_s). \quad (\text{B.2})$$

Then define the perturbation operator \mathbf{V} and the scattered field operator Ψ_s as,

$$\mathbf{V} = \mathbf{L} - \mathbf{L}_0, \quad (\text{B.3})$$

$$\Psi_s = \mathbf{G} - \mathbf{G}_0. \quad (\text{B.4})$$

The scattered field can be expanded in an infinite series with substituting \mathbf{G}_0 as an approximate \mathbf{G} ,

$$\Psi_s = \mathbf{G} - \mathbf{G}_0 = \mathbf{G}_0 \mathbf{V} \mathbf{G}_0 + \mathbf{G}_0 \mathbf{V} \mathbf{G}_0 \mathbf{V} \mathbf{G}_0 + \dots \quad (\text{B.5})$$

This infinite series is called Born series which is a basic formula for forward scattering field modeling. Consequently, the forward Born approximation for Ψ_s can be obtained by applying a linear truncation on the series. The result can be shown as,

$$\Psi_s \cong \mathbf{G}_0 \mathbf{V} \mathbf{G}_0. \quad (\text{B.6})$$

If the waves propagate in acoustic medium, the operators can be expressed as,

$$\mathbf{L}_0 = \frac{\omega^2}{c_0^2(\mathbf{r})} + \nabla^2, \quad (\text{B.7})$$

$$\mathbf{L} = \frac{\omega^2}{c^2(\mathbf{r})} + \nabla^2, \quad (\text{B.8})$$

$$\mathbf{V} = \mathbf{L} - \mathbf{L}_0 = -\frac{\alpha(\mathbf{r})}{c_0^2(\mathbf{r})} \omega^2. \quad (\text{B.9})$$

The $\alpha(\mathbf{r})$ in the equation (B.9) is defined as perturbation term, which satisfies $\frac{1}{c^2(\mathbf{r})} = \frac{1}{c_0^2(\mathbf{r})} [1 - \alpha(\mathbf{r})]$. Also, the Green's function operators satisfy $\mathbf{L}_0 \mathbf{G}_0 = -\mathbb{I}$ and $\mathbf{L} \mathbf{G} = \mathbb{I}$, which \mathbb{I} is the unit operator.

Left multiply \mathbf{L}_0 on Born approximation term B.6 to obtain $\mathbf{L}_0 \Psi_s = -\mathbf{V} \mathbf{G}_0$ and plug \mathbf{V} into it. The Born term turns out to be

$$\left(\nabla^2 + \frac{\omega^2}{c_0^2(\mathbf{r})} \right) \Psi_s(\mathbf{r}, \omega) = \frac{\alpha(\mathbf{r})}{c_0^2(\mathbf{r})} \omega^2 G_0(\mathbf{r}, \omega). \quad (\text{B.10})$$

Notice that Green's function here is in temporal frequency domain, so that the wavelet $A(\omega)$ can be multiplied on both sides of equation (B.10), which equals to convolve the wavelet in time domain. This step gives

$$(\nabla^2 + \frac{\omega^2}{c_0^2(\mathbf{r})})\Psi_s(\mathbf{r}, \omega)A(\omega) = \frac{\alpha(\mathbf{r})}{c_0^2(\mathbf{r})}\omega^2 G_0(\mathbf{r}, \omega)A(\omega). \quad (\text{B.11})$$

Introduce $\hat{p}_0(\mathbf{r}, \omega) = G_0(\mathbf{r}, \omega)A(\omega)$ and $\hat{p}_s(\mathbf{r}, \omega) = \Psi_s(\mathbf{r}, \omega)A(\omega)$, then substitute the p_0 and p_s into equation and inverse Fourier transform over two sides. The expression of equation (B.11) can be expressed in time domain as

$$(\nabla^2 - \frac{1}{c_0^2(\mathbf{r})}\frac{\partial^2}{\partial t^2})p_s(\mathbf{r}, t) = -\frac{\alpha(\mathbf{r})}{c_0^2(\mathbf{r})}\frac{\partial^2}{\partial t^2}p_0(\mathbf{r}, t). \quad (\text{B.12})$$

Finally, the equation (B.12) is obtained as the fundamental formula for time domain Born modeling. It is easy to acquire 2-D Born modeling equation as

$$\nabla^2 p_s(x, z, t) - \frac{1}{c_0^2(x, z)}\frac{\partial^2 p_s(x, z, t)}{\partial t^2} = -\frac{\alpha(x, z)}{c_0^2(x, z)}\frac{\partial^2}{\partial t^2}p_0(x, z, t), \quad (\text{B.13})$$

which is same as the equation given by equation (2.18).

References

- Alford, R. M., K. R. Kelly, and D. M. Boore. “Accuracy of finite-difference modeling of the acoustic wave equation.” *Geophysics* 39 (1974): 834–842.
- Araújo, F. V., A. B. Weglein, P. M. Carvalho, and R. H. Stolt. “Inverse scattering series for multiple attenuation: an example with surface and internal multiples.” *SEG Expanded Abstracts* (1994): 1039–1041.
- Baysal, E., D. D. Kosloff, and J. W. C. Sherwood. “Reverse time migration.” *Geophysics* 48 (1983): 1514–1524.
- Billette, F. and G. Lambaré. “Velocity macro-model estimation from seismic reflection data by stereotomography.” *Geophysical Journal International* 135 (1998): 671–680.
- Biondi, B. and G. Shan. “Prestack imaging of overturned reflections by reverse time migration.” *SEG Expanded Abstracts* (2002): 1284–1287.
- Bording, R. P. and L. R. Lines. *Seismic modeling and imaging with the complete wave equation*. Society of Exploration Geophysicists, 1997.

- Chattopadhyay, S. and G. McMechan. “Imaging conditions for pre-stack reverse-time.” *Geophysics* (2008): S81–S89.
- Claerbout, J. F. “Toward a unified theory of reflector mapping.” *Geophysics* (1971): 467–481.
- Clayton, R. W. and B. Engquist. “Absorbing boundary conditions for wave-equation migration.” *Geophysics* 45 (1980): 895–904.
- Clayton, R. W. and R. H. Stolt. “A Born-WKBJ inversion method for acoustic reflection data.” *Geophysics* 46 (1981): 1559–1567.
- Cohen, J. K., F. G. Hagin, and N. Bleistein. “Three-dimensional Born inversion with an arbitrary reference.” *Geophysics* 51 (1986): 1552–1558.
- Dessa, J. X., S. Operto, S. Kodaira, A. Nakanishi, G. Pascal, K. Uhira, and Y. Kaneda. “Deep seismic imaging of the eastern Nankai Trough (Japan) from multifold ocean bottom seismometer data by combined travelttime tomography and prestack acoustic modelling.” *Geophysical Journal International* 157 (2004): 1269–1296.
- Dragoset, B., E. Verschuur, I. Moore, and Bisley R. “A perspective on 3D surface-related multiple elimination.” *Geophysics* 75 (2010): 75245–75261.
- Fei, T., K. Fang, J. Ren, and S. A. Al-Dossary. “Reverse-time migration-the ultimate subsalt imaging algorithm, but how about the velocity sensitivity?” *Saudi Aramco Journal of Technology* Spring (2010): 8–10.

- Fleury, C. and R. Snieder. “Reverse-time-migration of multiply scattered waves.” *SEG Expanded Abstracts* (2011): 3382–3384.
- Fleury, C. and I. Vasconcelos. “Investigating an imaging condition for nonlinear imaging principle and application to reverse-time-migration artifacts removal.” *SEG Expanded Abstracts* (2010): 3338–3343.
- Kaelin, B. and A. Guitton. “Imaging condition for reverse time migration.” *SEG Expanded Abstracts* (2006): 2594–2598.
- Kelly, K. R. and K. J. Marfurt. *Numerical modeling of seismic wave propagation*. Society of Exploration Geophysicists, 1990.
- Liu, F., A. B. Weglein, K. A. Innanen, and B. G. Nita. “Extension of the non-linear depth imaging capability of the inverse scattering series to multidimensional media: strategies and numerical results.” *SBGf (Sociedade Brasileira de Geofísica) Expanded Abstracts* (2005): 1–5.
- Mayhan, J. D. and A. B. Weglein. “First application of Greens theorem-derived source and receiver deghosting on deep-water Gulf of Mexico synthetic (SEAM) and field data.” *Geophysics* 78 (2013): WA77–WA89.
- McMechan, G. A. “Migration by extrapolation of time dependent boundary values.” *Geophysics Prospecting* 31 (1983): 413–420.
- Muerdter, D. R., M. Kelly, and D. Ratcliff. “Understanding subsalt illumination through ray-trace modeling, Part 2: Dipping salt bodies, salt peaks, and nonreciprocity of subsalt amplitude response.” *The Leading Edge* (2001): 688–697.

- Muerdter, D. R., D. W. Ratcliff, W. K. Camp, and S. Bugosh. “Case studies of 3-D raytrace modeling for subsalt exploration and development in offshore Louisiana, Gulf of Mexico.” *SEG Expanded Abstracts* (1998): 13–18.
- Mufti, I. R. “Large-scale three-dimensional seismic models and their interpretive significance.” *Geophysics* 55 (1990): 1166–1182.
- O’Brien, M. J. and S. H. Gray. “Can we image beneath salt?” *The Leading Edge* (1996): 17–20.
- Press, W. H., S. A. Teukolsky, W. T. Vetterling, and B. P. Flannery. *Numerical recipes in FORTRAN: the art of scientific computing*. Cambridge University Press, 1986.
- Prieux, V., S. Operto, R. Brossier, and J. Virieux. “Application of acoustic full waveform inversion to the synthetic Valhall model.” *SEG Expanded Abstracts* (2009): 2268–2272.
- Rosenberg, M. V. “How much does salt obstruct the subsalt image?” *SEG Expanded Abstracts* (2000): 582–585.
- Shaw, S. A. and A. B. Weglein. *Frontiers of remote sensing information processing*. World Scientific Publishing Company, 2003.
- Weglein, A. B., F. V. Araújo, P. M. Carvalho, R. H. Stolt, K. H. Matson, R. T. Coates, D. Corrigan, D. J. Foster, S. A. Shaw, and H. Zhang. “Inverse scattering series and seismic exploration.” *Inverse Problems* (2003): R27–R83.

- Weglein, A. B. and S. H. Gray. “The sensitivity of Born inversion to the choice of reference velocity: a simple example.” *Geophysics* 48 (1983): 36–38.
- Weglein, A. B., S. A. Shaw, K. H. Matson, J. L. Sheiman, R. H. Solt, T. H. Tan, A. Osen, G. P. Correa, K. A. Innanen, Z. Guo, and J. Zhang. “New approaches to deghosting towed-streamer and ocean-bottom pressure measurements.” *SEG Expanded Abstracts* (2002): 1016–1019.
- Whitmore, D. N. “Iterative depth imaging by back time propagation.” *SEG Expanded Abstracts* (1983): 382–385.
- Wu, W., L. R. Lines, and H. Lu. “Analysis of higher-order finite-difference schemes in 3-D reverse-time migration.” *Geophysics* 61 (1996): 845–856.
- Zhang, J. and A. B. Weglein. “Extinction theorem deghosting method using towed streamer pressure data: analysis of the receiver array effect on deghosting and subsequent free surface multiple removal.” *SEG Expanded Abstracts* (2005): 2095–2100.